Article

Neuron

Cortical Output Is Gated by Horizontally Projecting Neurons in the Deep Layers

Highlights

- Simulations predict *in vivo* responses for major output cell type of the neocortex
- Simulations reveal strategy how to test the origins of cortical output empirically
- Manipulations confirm that deep-layer corticocortical neurons gate cortical output
- Gating of cortical output originates from deep-layer thalamocortical input stratum

Authors

Robert Egger, Rajeevan T. Narayanan, Jason M. Guest, ..., Suman Das, Christiaan P.J. de Kock, Marcel Oberlaender

Correspondence

marcel.oberlaender@caesar.de

In Brief

Egger, Narayanan, et al. describe the cellular and circuit mechanisms underlying the transformation of sensory-evoked thalamocortical input into fast and broadly tuned cortical output. The study provides a comprehensive multi-scale cortex model for studying streams of sensory-evoked excitation *in silico*.

Egger et al., 2020, Neuron *105*, 122–137
January 8, 2020 © 2019 The Author(s). Published by Elsevier Inc.
https://doi.org/10.1016/j.neuron.2019.10.011

CellPress

CellPress

Neuron
Article

Cortical Output Is Gated by Horizontally Projecting Neurons in the Deep Layers

Robert Egger,[1,3,4] Rajeevan T. Narayanan,[1,3] Jason M. Guest,[1] Arco Bast,[1] Daniel Udvary,[1] Luis F. Messore,[1] Suman Das,[2] Christiaan P.J. de Kock,[2] and Marcel Oberlaender[1,5,*]

[1]Max Planck Research Group In Silico Brain Sciences, Center of Advanced European Studies and Research (caesar), Ludwig-Erhard-Allee 2, 53175 Bonn, Germany

[2]Department of Integrative Neurophysiology, Center for Neurogenomics and Cognitive Research, VU Amsterdam, De Boelelaan 1085, 1081 Amsterdam, the Netherlands

[3]These authors contributed equally

[4]Present address: Long Laboratory, Neuroscience Institute, NYU School of Medicine, 435 East 30th Street, New York, NY 10016, USA

[5]Lead Contact

*Correspondence: marcel.oberlaender@caesar.de

https://doi.org/10.1016/j.neuron.2019.10.011

SUMMARY

Pyramidal tract neurons (PTs) represent the major output cell type of the mammalian neocortex. Here, we report the origins of the PTs' ability to respond to a broad range of stimuli with onset latencies that rival or even precede those of their intracortical input neurons. We find that neurons with extensive horizontally projecting axons cluster around the deep-layer terminal fields of primary thalamocortical axons. The strategic location of these corticocortical neurons results in high convergence of thalamocortical inputs, which drive reliable sensory-evoked responses that precede those in other excitatory cell types. The resultant fast and horizontal stream of excitation provides PTs throughout the cortical area with input that acts to amplify additional inputs from thalamocortical and other intracortical populations. The fast onsets and broadly tuned characteristics of PT responses hence reflect a gating mechanism in the deep layers, which assures that sensory-evoked input can be reliably transformed into cortical output.

INTRODUCTION

Pyramidal tract neurons (L5PTs) are located in layer 5 throughout the mammalian neocortex (reviewed in Ramaswamy and Markram, 2015). Along their extensive dendrite morphologies, L5PTs receive synaptic inputs from virtually all types of excitatory (Lefort et al., 2009) and inhibitory (Jiang et al., 2015) neurons within the same cortical area, from primary (Petreanu et al., 2009; Constantinople and Bruno, 2013) and higher-order thalamic nuclei (Audette et al., 2018; Viaene et al., 2011), and from several other cortical areas (e.g., Mao et al., 2011). Compared to other excitatory cell types in the neocortex, L5PTs have relatively sparse local axon projections (Narayanan et al., 2015), suggesting that they contribute only little to cortical computations. In turn, L5PTs project long-range axons to several subcortical brain areas. The subcortical targets typically depend on the cortical area the L5PTs reside in but vary substantially from cell to cell even within the same cortical area (Economo et al., 2018; Guo et al., 2017; Rojas-Piloni et al., 2017). L5PTs are hence considered as the major output cell type of the neocortex, whose function is to integrate feedforward thalamocortical (TC) excitation, with recurrent intracortical (IC) and top-down corticocortical (CC) inputs, and to broadcast the results of this integration to the relevant ensembles of downstream targets (reviewed in Harris and Shepherd, 2015).

Here, we study the origins of the L5PTs' general ability to respond with action potentials (APs) to a much wider range of stimuli compared to their TC and IC input neurons (Brecht et al., 2003; Brecht and Sakmann, 2002; Manns et al., 2004). The onset latencies of these broadly tuned output patterns can rival and even precede those in the major input layer 4 (Ito, 1992; Armstrong-James and Fox, 1987; Fox et al., 2003). It is believed that such fast onsets of cortical output patterns are driven directly by sensory-evoked synaptic inputs from the thalamus (Constantinople and Bruno, 2013). However, direct evidence that input from primary TC afferents is sufficient to reliably drive sensory-evoked APs in L5PTs has not been provided so far. Moreover, the broadly tuned characteristics of the fast onset responses were shown to require (additional) inputs from IC sources, which could, for example, originate from horizontally projecting neurons in the superficial layers (Wright and Fox, 2010). However, conclusive answers to the question—What are the cellular and/or circuit mechanisms underlying the transformation of sensory-evoked TC input into fast and broadly tuned cortical output?—remain presently unknown.

One major challenge for answering this question arises from the fact that activity patterns in L5PTs will in general reflect synaptic inputs from highly heterogeneous local and long-range populations. Moreover, L5PTs are among the biophysically most complex cell types of the mammalian brain. These neurons possess a large variety of voltage- and ligand-gated ion channels (Hay et al., 2011)—some of which are expressed exclusively in specific dendritic subdomains (Larkum et al., 1999a). The resultant non-linear intrinsic physiology thereby renders an additional challenge when trying to infer causality

 © 2019 The Author(s). Published by Elsevier Inc.
This is an open access article under the CC BY-NC-ND license (http://creativecommons.org/licenses/by-nc-nd/4.0/).

between activity patterns in populations that are presynaptic to a L5PT and its AP responses. Consequently, the logic and information content underlying responses in the major output cell type of the neocortex may only be revealed if the cellular origins, dendritic locations, and time points of synaptic input are known, and integration of these spatiotemporal input patterns could be studied with respect to the complex properties of the L5PTs' dendrites.

Here, we resolve these challenges by developing an approach that can disentangle how the interplay between synaptic, cellular, and network properties shapes sensory-evoked APs in L5PTs. We generated a multi-scale model of the TC and IC circuitry for the vibrissal-related part of rat primary somatosensory cortex (vS1) (i.e., barrel cortex; reviewed in Feldmeyer et al., 2013). The model is constrained at each scale by empirical data that were acquired consistently for animals of the same strain and age range, for morphologically identified cell types, and for one set of *in vivo* conditions (a link to download the model is provided in the STAR Methods). We demonstrate that the model allows performing simulations that mimic the sensory-evoked synaptic input patterns that impinge onto L5PTs during deflections of different individual whiskers. We show that the simulations allow investigating how active L5PT dendrites could in principle integrate and transform synaptic inputs, as evoked by different sensory stimuli, into AP output. The simulations thereby revealed experimental strategies for testing empirically the mechanistic origins underlying the transformation of sensory-evoked TC input into cortical output.

Consistent with the *in silico* predictions, we find *in vivo* that layer 6 corticocortical neurons relay sensory-evoked TC excitation horizontally across the entire cortical area and thereby provide virtually all L5PTs within vS1 with similarly strong and near-simultaneous synaptic input. We show that the spatiotemporal properties of this common drive, in conjunction with the intrinsic properties of the dendrites, function to amplify synaptic inputs that impinge additionally onto L5PTs at the time of stimulation.

RESULTS

Cell-Type-Specific Structural and Functional Constraints for Input Patterns to L5PTs

We had previously reported the AP activity of excitatory neurons that were recorded systematically across the depth of vS1 in anesthetized young adult rats (de Kock et al., 2007). Under these conditions, supra-threshold (i.e., AP) whisker receptive fields (wRFs) of individual neurons were determined at sub-millisecond precision with respect to stimulus onset by deflecting the somatotopically aligned principal whisker (PW), and of each of its eight surrounding whiskers (SWs), along the rostral-caudal axis with a piezoelectric bimorph (Figure 1A). The recorded neurons were filled *in vivo* with biocytin, which allowed for post hoc reconstruction of the neurons' precise columnar and laminar soma positions, dendrite morphologies, and IC axon projection patterns (Egger et al., 2012). In subsequent studies (Narayanan et al., 2015; Oberlaender et al., 2012a), we had used these reconstructions to establish classification criteria (Figure S1) for assigning *in vivo* recorded neurons from rat vS1 to the major axo-dendritic excitatory cell types of the neocortex (reviewed in Harris and Shepherd, 2015; Narayanan et al., 2017). Here, we combine the recording, reconstruction, and classification results and report wRFs with respect to objectively determined cell types (Figure 1B).

Whisker RFs were closely related to a neuron's axo-dendritic cell type (Figure 1C). In the superficial layers, the class of layer 2 pyramids (L2PYs) remained largely unresponsive to whisker deflections, whereas layer 3 pyramids (L3PYs) responded reliably with APs to the PW. In layer 4, spiny neurons (L4SPs) responded to the PW and the caudal SW within the same whisker row. Neurons of the rare class of L4PYs did not respond to the PW but to several SWs. In the deep layers, slender-tufted intratelencephalic (L5ITs) and corticothalamic neurons (L6CTs) had no reliable APs responses to whisker deflections. In contrast, L5PTs and corticocortical neurons in layer 6 (L6CCs) showed the most reliabe AP responses of all cell types. L5PTs had the broadest wRFs, responding to the PW and several SWs. L6CCs had wRFs that were similar to those of L4SPs. Under the present experimental conditions, whisker-evoked AP responses are hence dominated by four axo-dendritic cell types (L3PY, L4SP, L5PT, and L6CC), even though the somata of these neurons intermingle with those of the less reliably responding cell types within and across layers (i.e., L2PY, L4PY, L5IT, and L6CT).

Neurons across all layers responded similarly fast to PW and SW stimuli (median/25^{th}/75^{th} percentile of latency to first sensory-evoked AP: 14.3/13.3/18.4 ms). However, PW-evoked APs in L6CCs were the fastest (11.2/10.3/12.4 ms), followed by L4SPs (13.1/12.0/14.7 ms), L5PTs (14.3/13.6/16.2 ms), and L3PYs (14.8/13.7/20.1 ms). PW- and SW-evoked APs occurred near simultaneously in the deep-layer cell types (L6CC median: 10.3 versus 10.5 ms; L5PT: 13.6 versus 13.4 ms). In contrast, SW responses in layer 4 were significantly delayed compared to those evoked by the PW (L4SP: 12.0 versus 15.8 ms; Wilcoxon rank-sum test; difference: −4.4; 95% CI [−6.3, −2.1]; W = 168.5; p = 0.002).

Network Model Predicts Realistic Synaptic Input Patterns to L5PTs

To estimate the number and spatiotemporal distributions of synaptic inputs that impinge onto the dendrites of L5PTs during single whisker deflections, we used the cell-type-specific physiological and morphological data described above to generate and constrain an anatomically detailed model of the TC and IC excitatory networks in rat vS1. The network model is based on precise reconstructions of the geometry and somatotopic organization of cortical barrel columns (Egger et al., 2012) that represent the 24 major facial whiskers (i.e., macro vibrissae A1–E4; α-δ), measurements of the numbers and 3D distributions of all somata within the ventral posterior medial nucleus of the thalamus (VPM) and vS1 (Meyer et al., 2013), and the dendrite and/or axon reconstructions from *in vivo* labeled neurons that are representative for all major cell types in VPM and vS1 (Narayanan et al., 2015; Oberlaender et al., 2012a, 2012b; Rojas-Piloni et al., 2017). The network model provides predictions of connection probabilities between L5PTs and IC cell types, as

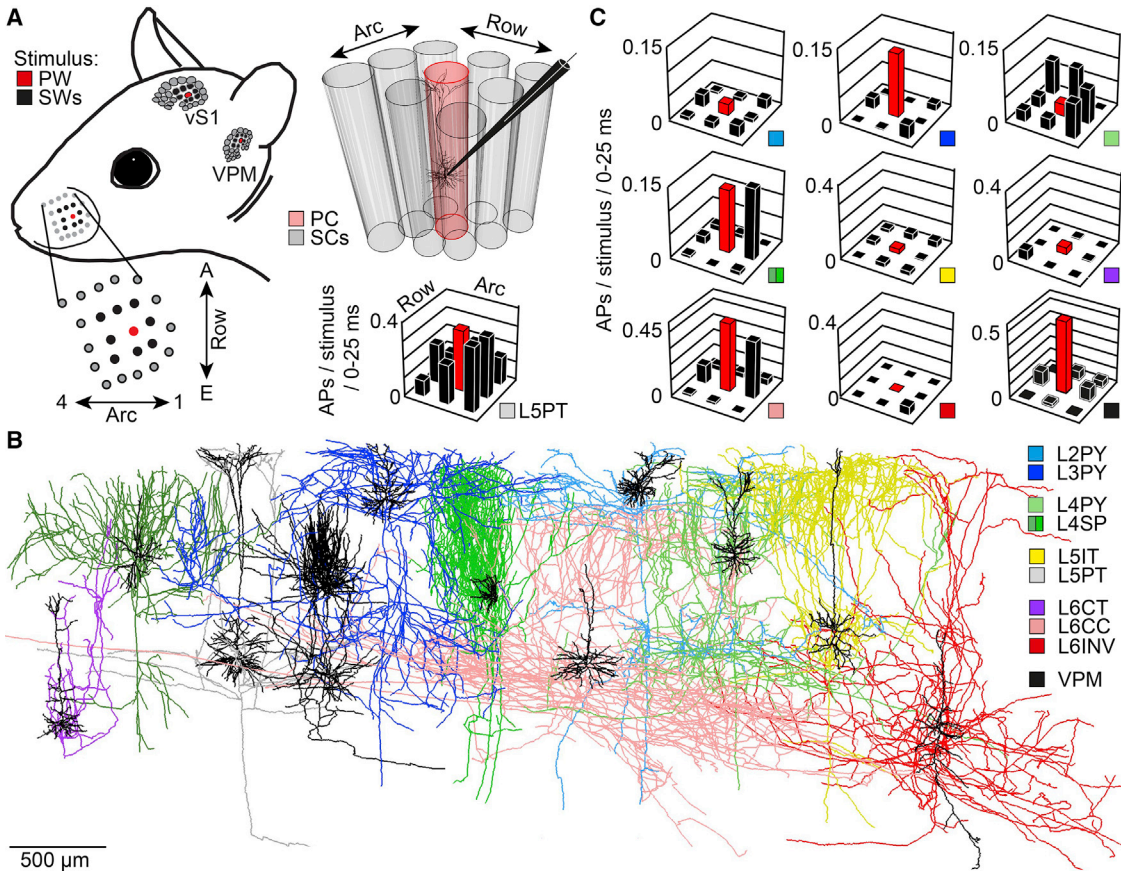

Figure 1. Cell-Type-Specific Structural and Functional Constraints

(A) Action potential (AP) whisker receptive fields (wRFs) were recorded in the vibrissal-related part of rat primary somatosensory cortex (vS1) by deflections of the principal (PW) and of each of its eight surrounding whiskers (SWs).

(B) Intracortical (IC) morphologies of *in vivo* labeled neurons that are representative for each axo-dendritic cell type in vS1 and for thalamocortical (TC) neurons in the ventral posterior medial nucleus (VPM). Example neurons represent pyramidal neurons in layer 2 (L2PY) (n = 16), layer 3 (L3PY) (n = 30), and layer 4 (L4PY) (n = 7); spiny stellates (L4ss) (n = 22) and star pyramids in layer 4 (L4sp) (n = 15); slender-tufted intratelencephalic (L5IT) (n = 18) and thick-tufted pyramidal tract neurons in layer 5 (L5PT) (n = 37); and corticothalamic (L6CT) (n = 13) and corticocortical neurons in layer 6 (L6CC) (n = 19). A subset of the L6CCs had apical-like dendrites that projected toward the white matter (WM) and was grouped as layer 6 inverted neurons (L6INV) (n = 5). L4ss and L4sp neurons were grouped as layer 4 spiny neurons (L4SP).

(C) Whisker RFs averaged across neurons of the same axo-dendritic cell type (L2PY [n = 7], L3PY [n = 7], L4SP [n = 8], L4PY [n = 2], L5IT [n = 13], L5PT [n = 9], L6CT [n = 5], L6CC [n = 6], and L6INV [n = 1]). Whisker RFs of VPM neurons were adopted from Brecht and Sakmann (2002).

See also Figure S1.

well as with VPM neurons, which match previously reported empirical data (Table S1).

We embedded the morphology of an *in vivo* labeled L5PT into the network model. The embedding provided realistic structural constraints about which neurons, depending on their respective cell type and soma location within VPM and vS1, can in principle form synaptic connections with the L5PT and where along its dendrites (Figure 2A). We combined the wRFs measurements for the major excitatory cell types of vS1 with those reported previously for VPM neurons (Brecht and Sakmann, 2002), which were acquired under the same experimental conditions. The cell-type-specific TC and IC wRFs were convolved with the respective number of neurons per cell type and cortical barrel column (or VPM barreloid) in the network model. Depending on the identity of the stimulated whisker, the convolutions provided functional constraints about which of the structurally possible connections to the L5PT could in principle provide functional input during each millisecond of the first 25 ms after whisker deflection (Figure 2B).

We sampled from the space of structurally and functionally plausible input neurons and generated 1,800 statistically possible spatiotemporal synaptic input patterns for each of the 24 major facial whiskers. The composition of input that impinges onto the L5PTs' dendrites is predicted to vary substantially, depending on the identity of the stimulated whisker, but to comprise in general neurons from all cell types and locations throughout VPM and vS1 (Figure 2C). Compared to periods preceding a stimulus (i.e., ongoing activity), the temporal profile post-stimulus of synaptic inputs to L5PTs shows an increase at time points that are largely independent of the identity of the

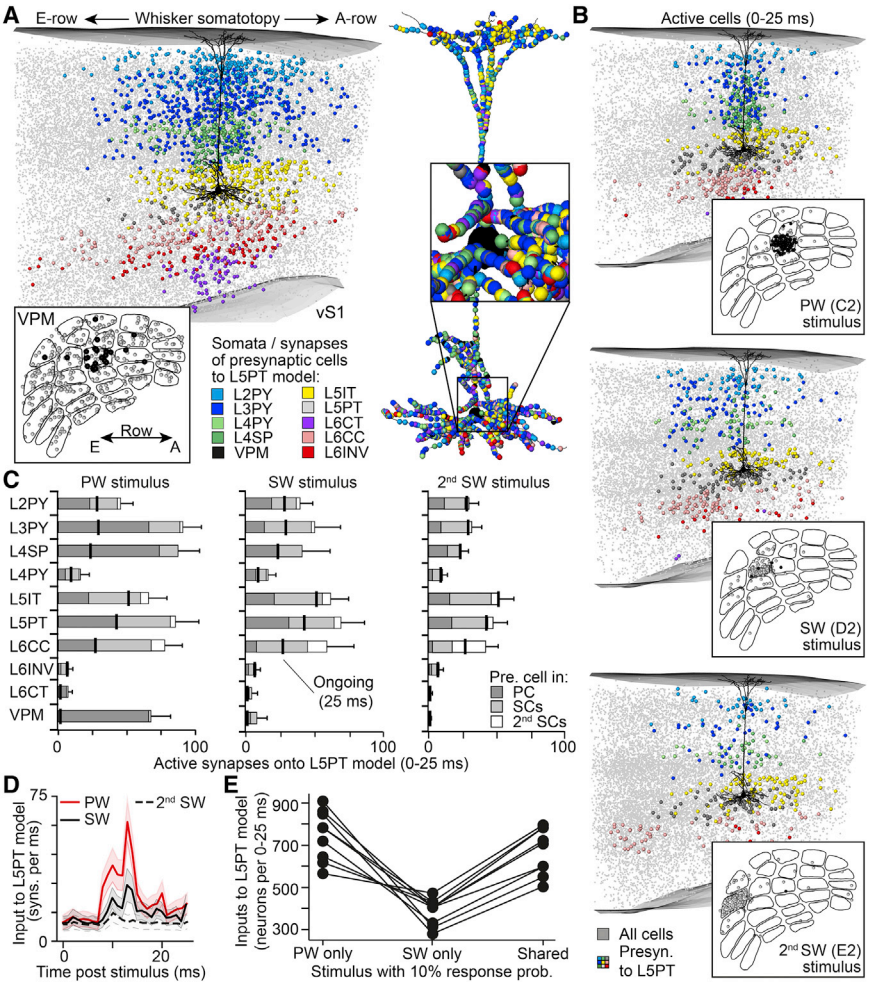

Figure 2. Network Model Predicts Realistic Synaptic Input Patterns to L5PTs

(A) Reconstruction of *in vivo* labeled L5PT (black) embedded into network model of rat vS1. Gray markers represent all somata of excitatory neurons. Colored markers represent soma distribution of exemplary input neurons to the L5PT. Colored markers in right panels represent exemplary synapse distribution originating from the neurons shown in the left panels.

(B) Exemplary soma distributions (colored markers) of neurons that provide synaptic input after deflections of the PW, one SW, or 2nd SW. Grey markers represent all neurons that elicit an AP during 0–25 ms post-stimulus.

(C) Quantification (mean ± SD) of the structurally and functionally plausible synaptic input patterns as shown in (B). Gray shadings denote the location of the presynaptic neurons in/around the barrel columns (or VPM barreloids) that are somatotopically aligned with the PW, SWs, or 2nd SWs (i.e., principal and surround columns [PCs and SCs]). Black lines denote the number of active synapses that each cell type contributes to 25 ms of ongoing activity.

(D) Temporal profile of the synaptic input patterns shown in (C). Lines and shaded areas denote the means and SDs across synaptic input patterns.

(E) Numbers of neurons predicted to provide reliable input to L5PTs during deflections of only the PW or SW or independent of the stimulated whisker (shared; see also Figure 4G in Varga et al., 2011).

See also Table S1.

stimulated whisker (Figure 2D). The hence predicted spatiotemporal synaptic input patterns display a degree of heterogeneity with respect to the identity of the stimulated whisker that is consistent with empirically determined synaptic wRFs (Varga et al., 2011), as reported for Ca^{2+} imaging of dendritic hotspots in mouse vS1 (Figure 2E).

Multi-scale Simulations Predict *In Vivo*-like Responses of L5PTs

We converted the network-embedded L5PT morphology into a biophysically detailed multi-compartmental model (Hay et al., 2011). The biophysical parameters were tuned until numerical simulations reproduced current injection-evoked somatic and/or dendritic sub- and supra-threshold responses that are characteristic for L5PTs (Table S2). The objectives for optimization were several properties of the membrane potential (Figure 3A) that parameterize Na^+ channel-based APs, back-propagating APs (bAPs), Ca^{2+} channel-based APs, and AP bursts, referred to as back-propagating action potential activated Ca(2+) spike (BAC) firing (Larkum et al., 1999b). The resultant optimal set of biophysical models yielded simulations in which the objectives were, on average, within 1.18 SDs of the respective empirical data (Table S3). From this optimal set, we selected a biophysical model that supported increasing AP frequencies when increasing the amplitude of sustained somatic current injections (Figure 3B). Synapses along the dendrites were converted into conductance-based models, containing both AMPA receptors (AMPARs) and NMDARs. For each cell type, the peak conductance of the synapses was tuned until the respective differences between simulated and empirically determined somatic unitary postsynaptic potential (PSP) distributions were minimized (Figure 3C; Table S4).

The multi-scale design of these L5PT models allows simulating how the locations and time points of synaptic inputs—as evoked by different sensory stimuli—are integrated by the complex intrinsic physiology of the dendrites and transformed into AP output at the soma (Video S1). These simulations may be considered to realistically mimic the specific *in vivo* conditions of single whisker deflections at subcellular, cellular, and network levels, if the anatomical, functional, biophysical, and synaptic model parameters are sufficiently constrained by the respective empirical data. To test whether this is the case, we simulated the integration of the structurally and functionally plausible synaptic input patterns without further optimization of any of the model parameters (Figure 3D). During periods of ongoing activity, the simulations predicted somatic

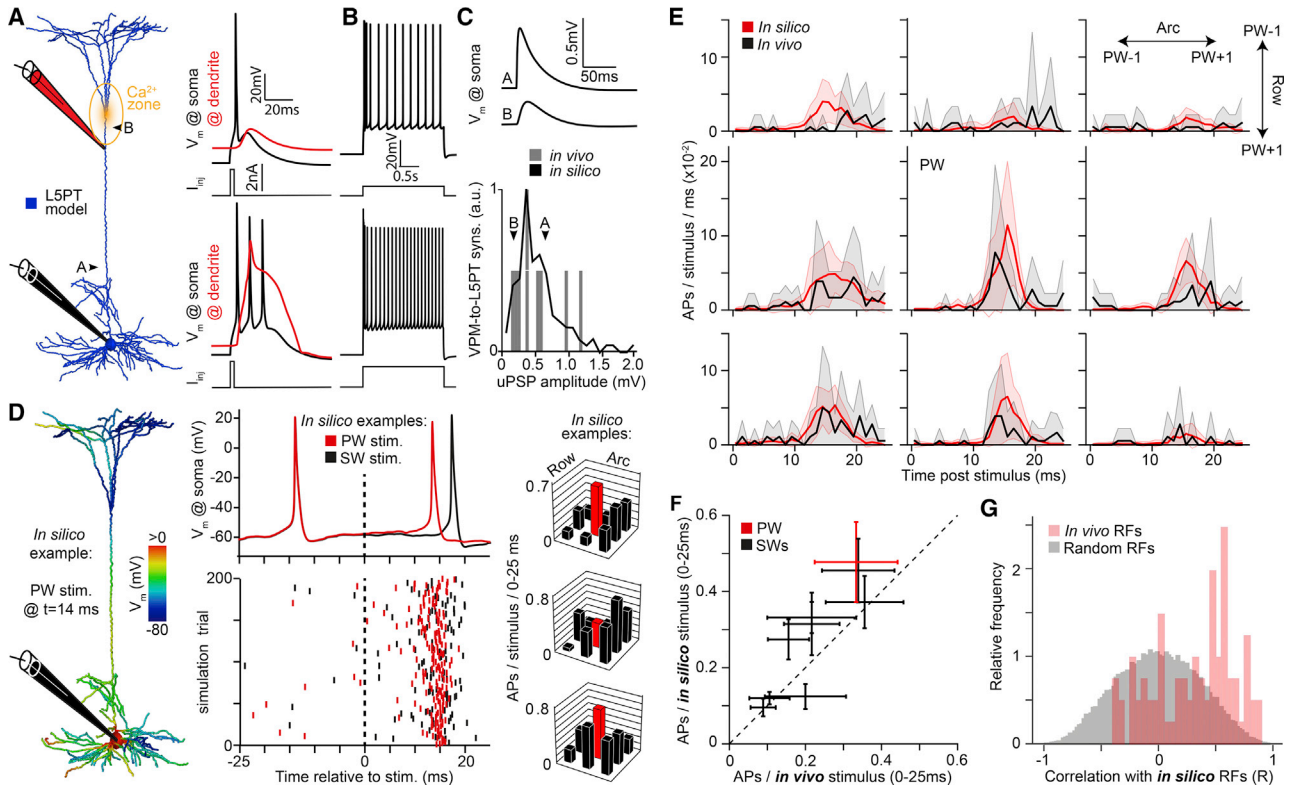

Figure 3. Multi-scale Simulations Predict *In Vivo* Responses of L5PTs

(A) Numerical simulations of current injections into the soma and/or Ca^{2+} channel dense region of the apical dendrite of a biophysically detailed multi-compartmental model of the L5PT shown in Figure 2.

(B) The model supports regular AP firing of increasing frequencies in response to sustained current injections of increasing amplitude.

(C) The peak conductance of synapses was optimized to match empirically determined unitary postsynaptic potential (uPSP) amplitude distributions (here: VPM-to-L5PT synapses).

(D) From left to right panels: membrane potential along the dendrites of the model for exemplary simulation of PW deflection. Somatic AP for exemplary simulations of PW and SW stimulation is shown. Raster plots of APs for 200 randomly selected simulation trials reflecting different plausible synaptic input patterns. Exemplary wRFs for three different L5PT models are shown.

(E) Post-stimulus time histograms (PSTHs) of APs during stimulation of the PW and the eight SWs. Solid lines and shaded areas represent the means and SDs across *in vivo* recorded L5PTs (n = 9) and L5PT models (n = 9), respectively.

(F) *In silico* versus *in vivo* average wRF of L5PTs. Error bars denote SEMs.

(G) Distribution of the correlations between *in vivo* and *in silico* wRFs (red) versus correlations with a null distribution (black) of synthetically generated random wRFs.

See also Tables S2, S3, and S4.

membrane potentials (−65.4 ± 4.1 mV) and AP rates (1.6 ± 1.4 Hz) that were within the respective ranges reported for L5PTs *in vivo* (Constantinople and Bruno, 2013; de Kock et al., 2007; Ito, 1992; Rojas-Piloni et al., 2017). During periods of sensory-evoked activity, the predicted response probabilities and AP latencies for deflections of the PW and any of the eight SWs were indistinguishable from the respective *in vivo* data (Figure 3E). Consequently, the shape of the average *in silico* wRF correlated well (Pearson's r = 0.88; 95% CI [0.52, 0.97]; t = 4.9; degrees of freedom [dof] = 7; p = 0.002) with its *in vivo* counterpart (Figure 3F). Even the variability of wRF shapes across L5PT models resembled the cell-to-cell variability observed *in vivo*. In contrast, synthetically generated random wRFs correlated significantly less with the *in vivo* data (Figure 3G; 0.31 ± 0.35 versus 0.002 ± 0.35; two-sided Wilcoxon rank-sum test; difference: 0.32; 95% CI [0.24, 0.41]; W = 2,661,834; $p = 7 \times 10^{-13}$).

Synchronous Input to Proximal Dendrites Drives the Fast Onsets of L5PT Responses

The similarities between the *in silico* predicted and *in vivo* recorded wRFs provided an opportunity to deconstruct AP responses into its constituent parameters or parameter combinations. We performed a principal component analysis of the dendritic locations, time points of activation, and cell-type-specific origins of the synaptic inputs that impinge onto the L5PT models during 0–25 ms after the stimulus onsets. The first principal component (PC_1) of these spatiotemporal synaptic input statistics separated well (*Z* score = 0.65) between simulation trials with and without AP responses (Figure 4A). 92% of

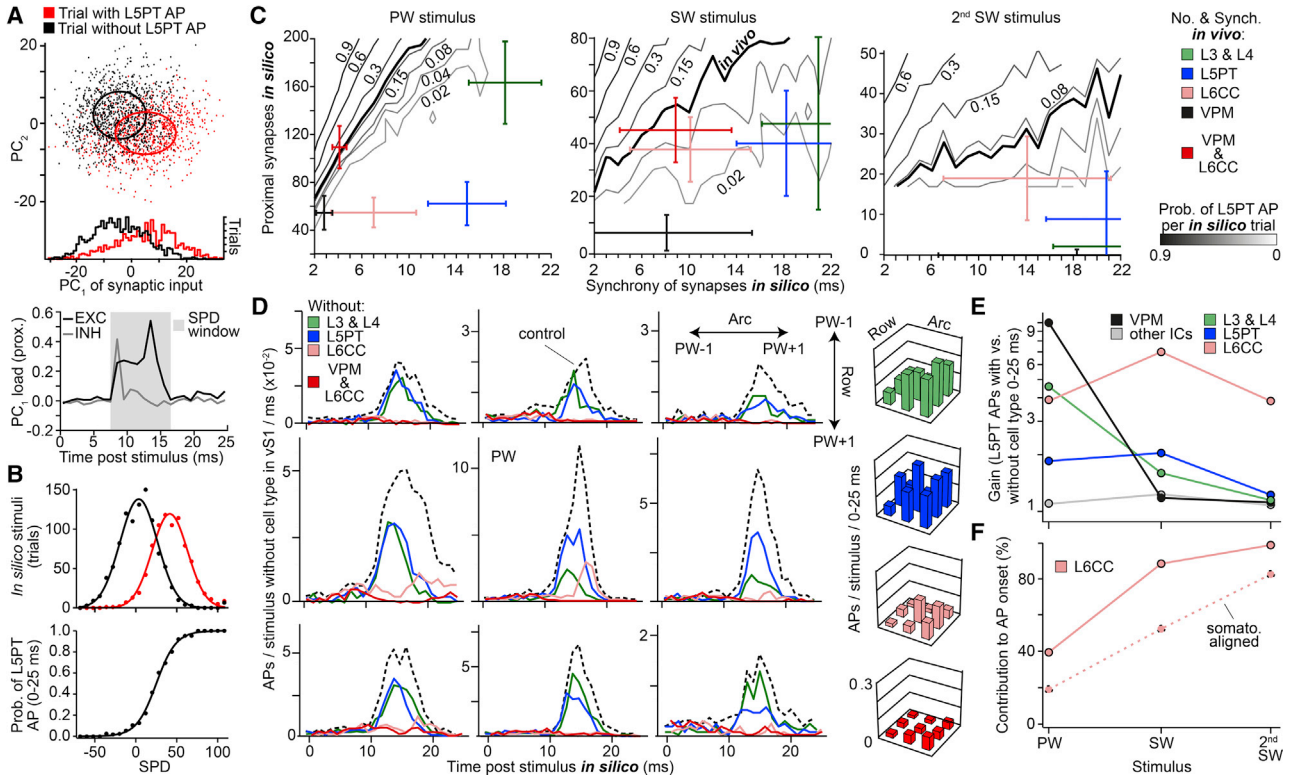

Figure 4. L6CCs Gate L5PT Output

(A) Principal component analysis of the spatiotemporal properties of synaptic input patterns to L5PT models. 92% of PC_1 reflect the net excitatory input to the proximal dendrites of L5PTs within a time window of 8–16 ms after the stimulus onset.

(B) Synchronous proximal drive (SPD) is an almost perfect predictor for the probability of AP responses in the simulations.

(C) Iso-probability plots of AP responses as a function of the number and synchrony of synaptic inputs to the proximal dendrites of L5PTs. Bold lines represent the average AP probability measured *in vivo* for PW, SW, and 2nd SW stimulations, respectively. Comparison between these general input/output relationships and the empirically determined properties of the TC and different IC cell types is shown (mean ± SD).

(D) PSTHs and average wRFs analogous to Figures 3D/3E but without stimulus-evoked inputs from the TC and different IC cell types.

(E) Increase in AP probabilities of L5PTs with versus without stimulus-evoked inputs from the TC and different IC cell types as shown in (D).

(F) Contribution from all versus somatotopically aligned L6CCs to the AP responses of L5PTs.

PC_1 reflected the number of excitatory and inhibitory synapses that were active between 8 and 16 ms post-stimulus and whose respective path length distances to the soma were less than 500 μm. The remaining 8% reflected inputs to more distal dendritic compartments, indicating that the non-linear properties of the apical dendrite contribute only little to the fast AP responses evoked by single whisker deflections. To test this interpretation, we extracted the net excitatory input (i.e., number of active excitatory minus inhibitory synapses) to the proximal dendrites within the 8- to 16-ms time window for each simulation trial and combined these properties into a single parameter (Figure 4B), which we defined as synchronous proximal drive (SPD). Consistent with the principal-component analysis, SPD was an almost perfect predictor for AP responses in the L5PT models (i.e., area under the receiver operating curve [AUROC] equals 1) during simulations of both PW and SW deflections (AUROC = 0.83 ± 0.03).

To explore the general relationships between the properties of SPD input and AP output, we performed additional simulations in which we systematically varied the number and synchrony of excitatory synaptic inputs that impinge onto the proximal dendrites. Iso-probability plots of AP responses illustrate these relationships and provide lookup tables for all possible input configurations that are necessary for SPD to underlie sensory-evoked APs in L5PTs (Figure 4C). We compared the SPD lookup tables with the structural and functional constraints determined empirically for the present conditions of single whisker deflections. Neither TC input from the VPM nor input from any single IC cell type would have the appropriate properties to account for the responses observed *in vivo*. However, combined TC and IC input from the VPM and L6CCs is predicted to be sufficiently numerous and synchronous to elicit APs in L5PTs at probabilities that match those evoked *in vivo* by deflections of the PW and SWs and even for 2nd SWs that are not adjacent to the PW.

To test the results of the principal component and SPD analyses, we repeated the *in silico* wRF mappings but sequentially deprived the different TC and IC cell types from their ability to respond to whisker stimulation. The simulations revealed that, in the absence of sensory-evoked inputs by L3PYs, L4SPs, or L5PTs, the overall AP response probabilities of the L5PT models

would be substantially reduced (Figure 4D). However, the fast onsets and broadly tuned characteristics of cortical output patterns would remain unchanged. In contrast, in the absence of sensory-evoked inputs by L6CCs, the simulations predicted that the fast APs of L5PTs in response to stimulations of any whisker would be completely abolished. Only the PW was predicted to maintain its ability to drive APs in L5PTs, however with substantially reduced response probabilities and delayed onsets. Depriving L5PTs additionally from TC inputs by the VPM abolished these residual PW-evoked AP responses. These results indicate that, for the present conditions of single whisker deflections, the SPD provided by L6CCs is not only sufficient but also necessary to account for the fast onsets and broadly tuned characteristics of cortical output patterns.

The SPD provided by inputs from TC or any other IC cell type is predicted to be in general insufficient to elicit AP responses in L5PTs. However, removing any of these inputs from the simulations reduced AP probabilities in response to PW and/or SW stimuli. We therefore quantified the gain with respect to the identity of the stimulated whisker that each of the TC and IC populations contribute to AP responses of L5PTs (Figure 4E). The strongest contribution to AP responses that are evoked by the PW is predicted to arise from TC inputs, followed by IC inputs from L3PYs and L4SPs. The contributions by TC inputs decrease rapidly with increasing distance between the stimulated whisker and the PW. Consequently, responses during SW deflections are predicted to be dominated by inputs from IC cell types and to be even independent of TC inputs during 2nd SW deflections. The contributions by IC inputs also decrease with distance to the PW. In contrast, the gain provided by L6CCs does not decrease with distance. Instead, inputs from L6CCs are predicted to provide equally strong contributions to AP responses in L5PTs, independent of the identity of the stimulated whisker. Relative to the respective inputs from any other TC/IC population, the contributions by inputs from L6CCs thereby increase with distance from the PW. For the present experimental conditions, L6CCs are hence predicted to account for 99% of the fast AP responses during 2nd SW deflections, compared to 39% during PW deflections (Figure 4F).

L6CCs Underlie the Fast Onsets and Broadly Tuned Characteristics of L5PT Responses

Deconstructing the *in silico* wRFs into their constituents revealed that L6CCs provide input to the proximal dendrites of the L5PT models that is sufficiently strong and synchronous to drive APs, no matter whether the PW or any of the SWs or 2nd SWs are deflected. In the absence of additional inputs, L6CCs are thus predicted to drive unspecifically tuned broad wRFs, where virtually all L5PTs throughout vS1 would be able to respond with similarly fast APs to stimulations of any whisker. However, additional inputs from TC and other IC cell types will contribute to the SPD that is provided by the L6CCs and thereby increase the response probabilities of L5PTs and shape their RFs accordingly. The fast component of cortical output patterns is hence predicted to originate from a gating mechanism, where unspecific amplification via inputs from L6CCs is required to transform stimulus-specific inputs from TC and other IC cell types into AP output. Our simulations reveal a strategy that should provide direct access to empirically test the existence of the gating mechanism. For the present experimental conditions, fast APs in L5PTs that are evoked by 2nd SW stimuli are predicted to originate almost exclusively from inputs by L6CCs. The vast majority of these driver neurons should be located within and around the respective somatotopically aligned 2nd surround barrel column (2nd SC) (Figure 4F), and their SPD should be sufficient to elicit AP responses with probabilities that are, however, one order of magnitude lower compared to those that reflect amplification of additional TC and/or IC inputs during PW or SW stimuli.

We tested this strategy first by repeating the *in silico* wRF mappings but now only deprived L6CCs within a 2nd SC from their ability to respond to whisker stimuli (Figure 5A). The manipulation abolished any of the fast APs in response to the 2nd SW. In contrast, the simulation results for deflections of any other whisker were not affected. Depriving all excitatory neurons within the 2nd SC from their ability to respond to whisker stimuli, except for the L6CCs, did not alter any of the simulation results. The *in silico* manipulations hence reveal that depriving L5PTs specifically from inputs by L6CCs that are located within a 2nd SC should remove the related 2nd SW from their wRFs, without affecting the responses to any other whisker. To test these predictions, we repeated the *in vivo* wRF mappings for L5PTs and combined the recordings with injections of the $GABA_A$ agonist muscimol. Measuring local field potentials (LFPs) across the depth of vS1, and in response to deflections of several individual whiskers, allowed placing both the recording and injection pipettes at precise columnar and laminar positions (Figure S2A). Injection pipettes were positioned within a cortical barrel column that represented a 2nd SW with respect to the PW at the recording site and at a cortical depth where L6CCs are most abundant. Once both pipettes were placed appropriately, we recorded responses from L5PTs to deflections of their PW, the 2nd SW, and the intermediate SW before and after muscimol injections into the respective 2nd SC (Figure 5B).

The muscimol injections abolished the IC activity within a volume of less than 100 μm in diameter (Figure S2B). The functional effect of muscimol degraded gradually with distance and did not extend further than ~300 μm from the injection site. The manipulated volumes hence comprised parts of deep layer 5 (i.e., L5B) and upper layer 6 (i.e., L6A) and remained largely restricted to the 2nd SC. Consequently, in addition to L6CCs, the manipulations also affected L5PTs and L6CTs. However, in contrast to the elaborate horizontal axon projections of L6CCs, axons of L5PTs and L6CTs remain largely restricted to the volume of a single cortical barrel column. The separation between the injection and recording pipettes of ~1 mm hence assures that only L6CCs, but not neurons from other cell types that are affected by the pharmacology, could provide direct synaptic input to the recorded L5PTs (Figure S2C). Moreover, the amplitudes of LFPs that reflect VPM axons that pass through the manipulated volumes were not significantly altered by the pharmacology ($n = 3$; two-sided t test; unpaired; $p > 0.15$). Hence, TC input to the upper layers, and in particular to layer 4, remained unaffected. The *in vivo* pharmacology experiments can thus be considered to resemble the configuration of the *in silico* manipulations, where L5PTs were deprived exclusively from sensory-evoked inputs by L6CCs in the 2nd SC.

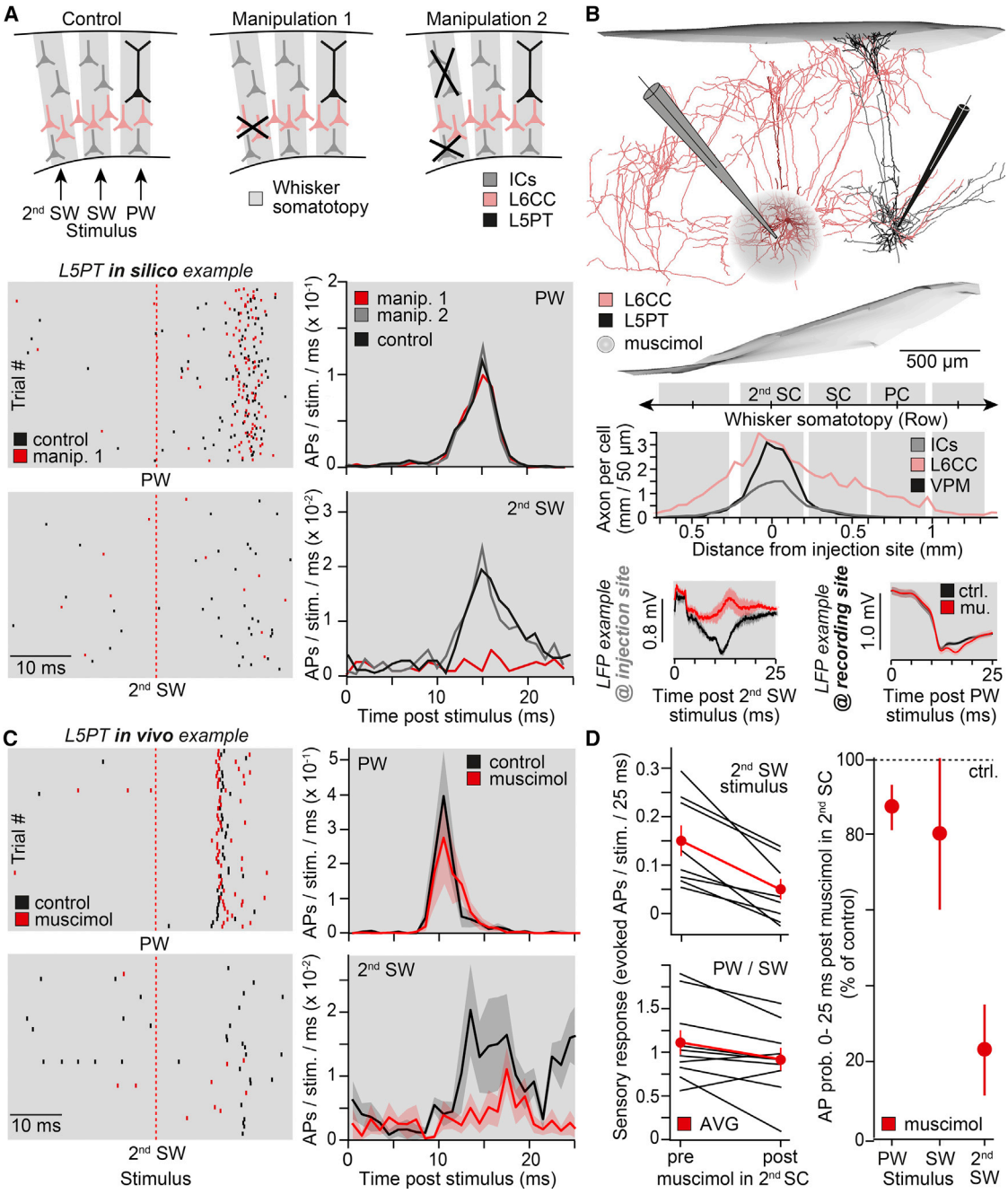

Figure 5. Local Deactivation of L6CCs Affects L5PT Responses throughout vS1

(A) Simulations for two different manipulation scenarios: L6CCs or all other neurons in/around a 2nd SC were deprived from their ability to respond to whisker stimuli. Raster plots represent APs of the L5PT models for 200 randomly selected simulation trials in control and manipulation 1 scenarios, respectively. PSTHs for PW and 2nd SW stimuli in control and both manipulation scenarios are shown.

(B) Strategy to test the predictions empirically. Recording whisker-evoked local field potentials (LFPs) allows placing of muscimol injection and recording pipettes at precise columnar and laminar positions. Top to bottom panels: L6CC and L5PT labeled in the same animal are shown. Axonal extent in the deep layers of L6CCs versus TC and other IC cell types is shown. Example LFPs (mean ± SEM) before and after muscimol injections recorded via the injection and recording pipettes, respectively, are shown.

(C) Exemplary AP responses evoked by PW or 2nd SW stimuli and PSTHs across L5PTs (mean ± SEM; 2nd SW: n = 8; PW: n = 5).

(D) Left panels: APs per L5PT before and after muscimol injections (red: mean ± SEM) in response to a 2nd SW (n = 8) and non-manipulated PW or SW (n = 5, respectively). Right panel: effect of muscimol on AP response probabilities of L5PTs is shown (mean ± SEM).

See also Figure S2.

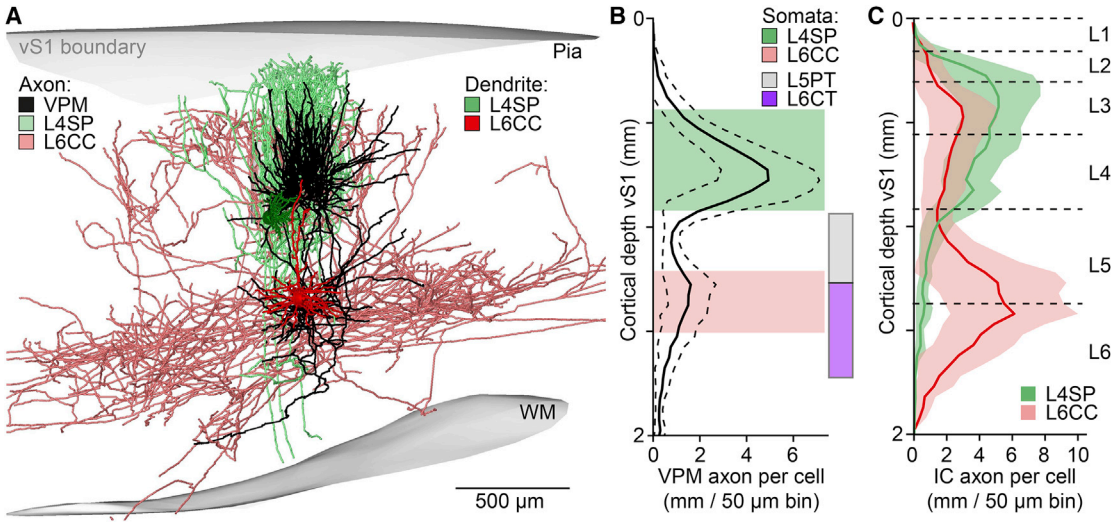

Figure 6. L6CCs Cluster around Deep-Layer Terminal Fields of Primary TC Axons

(A) Examples of *in vivo* labeled L4SP, L6CC, and VPM axon in rat vS1.

(B) Somata of L4SPs (n = 37) and L6CCs (n = 14) cluster around the two innervation peaks of VPM axons (n = 14; mean ± SD). Somata of L6CCs intermingle with those of the subcortically projecting L5PTs (n = 38) and L6CTs (n = 13).

(C) L4SP and L6CC axons (mean ± SD; same cells as in B) versus cytoarchitectonic layer borders (Meyer et al., 2013).

Following the muscimol injections, the ability to elicit fast APs in response to the manipulated 2nd SW was abolished in all of the recorded L5PTs (Figure 5C). In contrast, both PW and SWs maintained their ability to evoke reliable and fast AP responses. Moreover, in agreement with the gain analysis of the *in silico* wRFs, which predicted that L6CCs within the 2nd SC should contribute 82% to 2nd SW-evoked APs, response probabilities were reduced *in vivo* by 78% ± 10% (n = 8; mean ± SE; Wilcoxon signed-rank test: median = 0.095; 95% CI [0.05, 0.16]; W = 36; p = 0.008; Figure 5D). Because L5PTs within the (2nd) SC can be either directly or indirectly affected by the manipulation, AP probabilities in response to the PW and SW were slightly reduced at trend level (PW and SW, n = 5 and n = 5; Wilcoxon signed-rank test: median = 0.18; 95% CI [6 × 10^{-5}, 0.38]; W = 47.5; p = 0.05), which is also consistent with the gain analysis for L5PTs. To control for the possibility that neurons of other cell types could contribute to the fast 2nd SW-evoked responses in L5PTs, we repeated the manipulations but targeted the muscimol injections to horizontally projecting neurons in layer 2/3 or deep layer 6 of the 2nd SC (Figures S2D and S2E). These manipulations neither affected the L5PTs' ability to elicit fast APs in response to the PW, SW, or 2nd SW (Figure S2F) nor were the response probabilities significantly altered for deflections of any of the whiskers (PW/SW: n = 12; Wilcoxon signed-rank test: median = 0.03; 95% CI [−0.24, 0.22]; W = 45; p = 0.68 and 2nd SW: n = 6; Wilcoxon signed-rank test: median = 0.03; 95% CI [−0.06, 0.08]; W = 17; p = 0.22).

L6CCs Are Strategically Placed around TC Axons to Respond First to Sensory Stimuli

We explored the origins of the reliable and sufficiently synchronous drive that L6CCs provide to L5PTs. Somata of L6CCs were found exclusively around the density peak of VPM axons (median/25th/75th percentile of soma depths: 1,358/1,317/1,391 µm) at the border between cytoarchitectonic layers 5 and 6 (Figure 6A). L6CCs are hence equally abundant in lower layer 5 and upper layer 6 (range: 1,211–1,503 µm), where they intermingle with somata of L5PTs (938–1,273 µm) and L6CTs (1,262–1,722 µm), respectively (Figure 6B). Somata of polymorphic L6CCs (i.e., L6INVs) are restricted to deeper regions of layer 6 (1,424–1,610 µm). Even though their somata intermingle, L6CCs can be easily distinguished from the other deep layer cell types by their morphological properties (Figure S1). The apical dendrites of L6CCs terminate in layer 4 without forming a tuft. Moreover, compared to all other cell types, L6CCs have the most extensive axon projection patterns, reaching path lengths within vS1 (11.83 ± 5.46 cm) that exceed those of L5PTs and L6CTs by almost one order of magnitude (1.99 ± 1.38 cm) and which span across the deep layers of almost the entire cortical area (Figure 6C).

The clustering around the terminal fields of VPM axons suggests that L6CCs might be strategically placed to receive TC input that is sufficiently strong to drive reliable sensory-evoked APs. To test this hypothesis, we measured the path length that APs need to travel along VPM axons before they reach the L6CCs and L4SPs, respectively. Combined with conduction velocity measurements (Salami et al., 2003), the analysis predicted that sensory-evoked excitation reaches the L6CCs 3.0 ± 1.7 ms earlier than the L4SPs (Figure 7A). These delay predictions were consistent with our *in vivo* wRF data (Figure 7B). On average, AP onsets of L6CCs in response to both PW (Figure 7C) and SW deflections (Figure S3) preceded those in all other excitatory cell types by 3 ms—including L4SPs and L5PTs. To study whether such fast activation of deep-layer neurons, as consistently observed in anesthetized (Carvell and Simons, 1988; Ito, 1992; Armstrong-James and Fox, 1987; Fox et al., 2003) and sedated

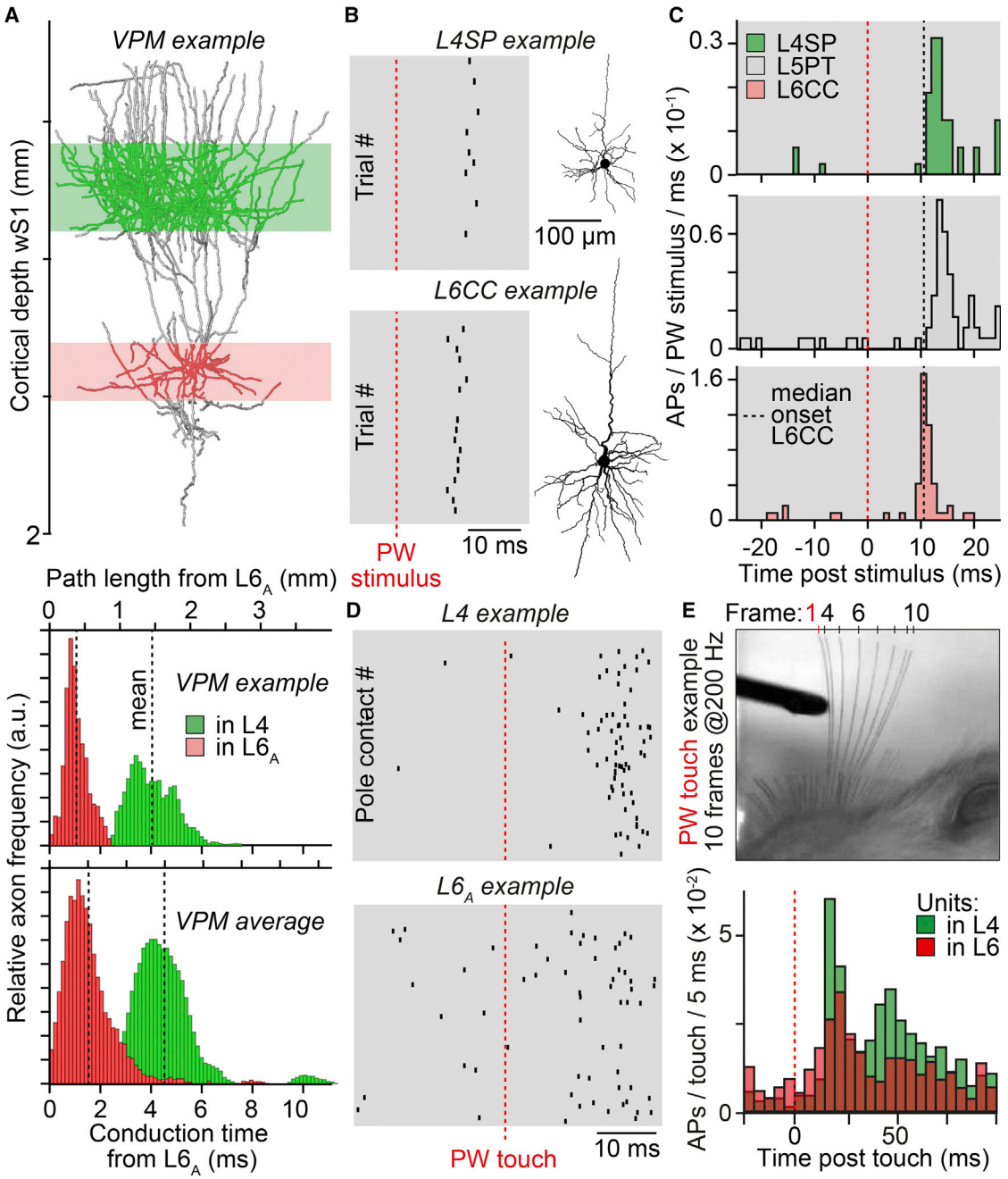

Figure 7. TC Input Evokes Responses in L6CCs that Precede Those in All Other Cell Types

(A) Example of *in vivo* labeled VPM axon (top panel), whose path length distribution was quantified with respect to the deepest location where L6CCs are found (here referred to as layer 6_A). Path lengths were divided by the IC conduction velocity (0.33 m/s; Salami et al., 2003) of TC axons (middle panel). Average conduction time of VPM axons (n = 14) to layer 6_A and 4, respectively (bottom panel), is shown.

(B) AP responses evoked by PW stimuli in exemplary L4SP and L6CC.

(C) PSTHs of PW-evoked APs in morphologically identified L4SPs (n = 8), L5PTs (n = 9), and L6CCs (n = 6).

(D) Example of simultaneously recorded single units in layers 4 and 6_A, which show reliable AP responses after PW contact with a pole during exploratory whisking.

(E) Top panel: whisker positions after exemplary touch. Bottom panel: PSTHs of touch-evoked APs of single units in layers 4 (n = 5) and 6 (n = 8) are shown. See also Figure S3.

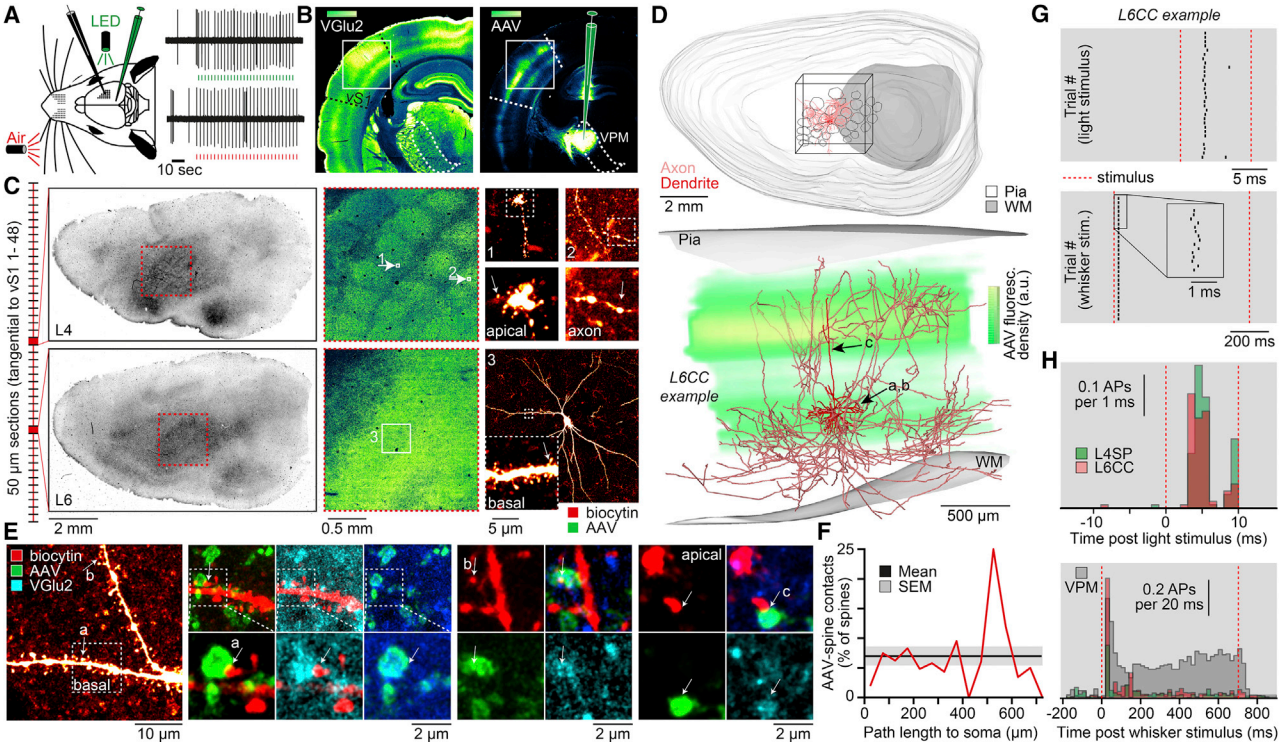

Figure 8. L6CCs Receive Strong Convergent TC Input

(A) Example of cell-attached recording in vS1 of AAV-injected brain representing the L6CC shown in (C)–(G).

(B) Coronal section through vS1 of exemplary AAV-injected animal immunolabeled for the vesicular glutamate transporter 2 (VGlu2).

(C) Following the recordings, brains were cut into consecutive sections, tangentially to vS1 (left panels). Maximum z-projections from confocal image stacks show AAV-labeled VPM terminals (middle panels) and biocytin-labeled morphologies (right panels).

(D) 3D reconstruction of the L6CC. Bottom panel: reconstruction superimposed with fluorescent density distribution of AAV labeling is shown.

(E) Super-resolution microscopy of dendritic spines that overlap with AAV/VGlu2-positive boutons.

(F) Fraction of spines (n = 4,789) contacted by VPM boutons.

(G) Raster plots of APs in response to light and airpuff stimulations.

(H) PSTHs of light-evoked APs across L4SPs and L6CCs (mean ± SD of AP onset: 4.6 ± 0.7 ms, n = 4 versus 4.4 ± 0.8 ms, n = 4) and of airpuff-evoked APs (including VPM neurons; n = 7).

See also Figure S4.

animals (Constantinople and Bruno, 2013), also extends to awake conditions, we simultaneously recorded APs from several single units across the depth of vS1 of head-fixed, behaving rats. Here, we restricted our analyses to reliably responding units in layer 4 and upper layer 6. Rats were not trained to perform tactile behavior. Instead, sensory input was provided by whisker contact with a pole that was placed within range during periods when animals voluntarily explored their environment by rhythmically moving the PW. During these "naïve" conditions, near-simultaneous onsets of AP responses were observed for single units in layers 4 and 6 (Figure 7D). Consistent with the delay predictions and the latency differences in anesthetized rats, touch-evoked AP onsets in layer 6 preceded those in layer 4, on average by 3.5 ms within the same animal (median/25th/75th delay across animals: 3.7/2.1/4.1 ms; Wilcoxon rank-sum test; difference: 3.0; 95% CI [1.3, 5.0]; W = 6,782; p = 3 × 10^{-4}; Figure 7E).

To test directly whether L6CCs receive convergent input from primary TC axons that is similarly strong compared to L4SPs, we quantified the respective degrees to which these two populations form monosynaptic connections with VPM axons and investigated whether these TC inputs can indeed drive reliable AP responses during *in vivo* conditions. We combined cell-attached recordings in anesthetized rats with injections of an adeno-associated virus (AAV) into the thalamus (Figure 8A). The AAV injections infected the VPM-to-vS1 pathway (Figure 8B) and expressed channelrhodopsin (ChR2) and a fluorescent marker (mCherry) within 79% ± 3% of the TC synapses (i.e., AAV-infected axonal boutons co-expressed the vesicular glutamate transporter 2 [VGlu2]). The AP activity of individual neurons across layers 4–6 was measured in response to a 10 ms flash of green light onto the cortical surface and a 700 ms low-pressure airpuff that deflects all whiskers caudally. The recorded neurons were filled with biocytin, which allowed for post hoc reconstruction of their morphologies, classification into axo-dendritic cell types, and detection of VPM synapses along their dendrites (Figures 8C and S4A).

We selected a L6CC from this dataset that was representative for the structural properties that characterize this class of neurons: the soma was located within the deep TC input stratum

right at the layer 5/6 border, the apical dendrite terminated without a tuft in layer 4, and the IC axon shows extensive horizontal projections throughout the deep layers (Figure 8D). Moreover, the high quality of biocytin labeling allowed detecting whether each of the neuron's dendritic spines is contacted by an AAV-labeled bouton. Subsequent super-resolution microscopy revealed whether these contact sites represent putative TC synapses (i.e., co-localization of VGlu2; Figures 8E and S4B). 95% ± 2% of the AAV-labeled swellings that were identified as axonal boutons co-expressed VGlu2 (Figure S4C). Along both basal and apical dendrites, on average, 7% ± 2% of the spines were contacted by AAV-labeled boutons (Figure 8F). Given the efficacy of the AVV, we hence estimate that 6%–10% of the excitatory inputs to L6CCs originate from the VPM. Similar fractions of 10% ± 4% have been reported for L4SPs of rat vS1 (Schoonover et al., 2014). Supporting these anatomical observations, light stimulation of VPM synapses elicited APs in the L6CCs that were equally reliable and as fast as those in the L4SPs (Figure 8G). The same neurons also responded reliably to the multi-whisker stimulus. Responses in L6CCs were, however, more reliable compared to those of L4SPs and even rivaled the reliability of relay cells in the VPM (Figure 8H).

DISCUSSION

We provide several lines of computational and empirical evidence that reveal the organizational principles by which the interplay between TC and IC populations shape sensory-evoked activity patterns in the deep layers of the neocortex. Similar to L4SPs, which cluster around the dense terminal fields of VPM axons (Feldmeyer et al., 2013), we find that L6CCs cluster around the second innervation domain of VPM axons at the layer 5/6 border. Even though the deep layers are less densely innervated by VPM axons (Oberlaender et al., 2012a; Wimmer et al., 2010), we show that synaptic inputs from these primary TC fibers converge similarly strong onto L4SPs and L6CCs. These results are consistent with paired recordings in rat VPM and vS1 (Constantinople and Bruno, 2013), which revealed that the majority of connected neurons across the deep layers are located within ±100 μm around the layer 5/6 border. Neurons at these depths had also the largest PW-evoked PSPs within the deep layers. Being strategically placed to receive direct TC input that is sufficiently strong to reliably drive sensory-evoked APs, we conclude that L6CCs represent the postsynaptic part of a deep TC input stratum.

This conclusion does not imply that TC input is restricted to L6CCs but rather that TC input will be less sufficient to drive reliable APs in the other deep-layer cell types. Compared to L6CCs, L6CTs were shown to receive less convergent and weaker synaptic inputs from primary thalamic nuclei (Crandall et al., 2017; Vélez-Fort et al., 2014). Moreover, their intrinsic physiological properties render L6CTs as less excitable than L6CCs (Crandall et al., 2017; Kumar and Ohana, 2008; Vélez-Fort et al., 2014). Resulting in smaller sensory-evoked PSPs and relative hyperpolarization (Constantinople and Bruno, 2013), these properties are likely the reason why L6CTs remain unresponsive to whisker deflections and to sensory stimulation in general (Lee et al., 2008; but see Brown et al., 2019). Compared to L6CTs, L5PTs have membrane potentials during periods of ongoing activity that are significantly closer to AP threshold, and these neurons can receive stronger convergent synaptic inputs from VPM axons, in particular, when they are located in deep layer 5 (Constantinople and Bruno, 2013). In combination with pharmacological deactivation of layer 4, which neither affected the onset latencies nor strengths of PW-evoked PSPs of neurons around the layer 5/6 border, it was hence suggested that direct TC input could be sufficient to drive AP responses in L5PTs. However, we show that, despite being more depolarized, amplification of TC inputs via L6CCs is required to drive fast and reliable APs in L5PTs. Because PW-evoked responses in L5PTs will in general reflect combinations of VPM and L6CC inputs, manipulations of the upper layers are insufficient to conclude that cortical output is driven directly by TC input.

Amplification via inputs from L6CCs is not restricted to PW stimuli. Because of their extensive horizontal axon projections, L6CCs relay sensory-evoked excitation from the local thalamorecipient volume to virtually all L5PTs throughout vS1. The gain for AP output that arises from this input is predicted to be independent of the stimulated whisker and to be sufficient to drive APs in L5PTs, even if no additional inputs are provided. The predictions are consistent with several of our empirical observations. Onset latencies of sensory-evoked APs in L5PTs can be similarly short no matter whether the PW or any of the SWs or 2nd SWs are stimulated (see also Manns et al., 2004). Moreover, these fast AP responses in L5PTs occur near simultaneously with those in L4SPs (see also Constantinople and Bruno, 2013) and are hence consistently delayed with respect to APs in L6CCs (see also Carvell and Simons, 1988). The amplitudes (i.e., AP probabilities) of broadly tuned cortical output patterns are, however, not solely determined by L6CC inputs but reflect the degree to which L6CCs amplify additional input patterns. In contrast to PW stimuli, SW-evoked APs are predicted to reflect amplification of inputs primarily from IC cell types (i.e., here from L5PTs and L3PYs). Our result that the broad wRFs of L5PTs originate from IC circuits, not from direct TC input, is consistent with previous reports. VPM neurons that respond to deflections of SWs do so with longer onset latencies and less synchrony compared to those that respond exclusively to the PW (Brecht and Sakmann, 2002). Moreover, depriving VPM neurons from their ability to respond to SWs had no impact on the wRFs of layer 5 neurons (Kwegyir-Afful et al., 2005).

We hence conclude that, by shaping the organizational principles of a deep TC input stratum, L6CCs provide similarly strong, sufficiently synchronous, and stimulus-unspecific synaptic drive to the proximal dendrites of L5PTs throughout the cortical area, which assures that additional inputs from TC and other IC populations can be reliably transformed into AP output. What could be the computational benefit of such a gating mechanism? If L5PTs would be driven exclusively by TC input, the fast component of sensory-evoked cortical output patterns would simply reflect a direct copy of the stimulus representation in the thalamus. In contrast, the gating mechanism allows L5PTs across vS1 to simultaneously integrate and transform sensory-evoked inputs from differently tuned TC populations into cortical output. As a population, L5PTs could thereby encode the entire

(multi-whisker) stimulus information that was simultaneously provided by the thalamus (Ramirez et al., 2014). The gating mechanism also assures that the AP probability of each L5PT reflects a combination of all inputs that impinge onto the neuron at the time of stimulation. L5PTs could thus integrate the current state of their respective local (and long-range) input populations with stimulus information and thereby provide subcortical circuits with an integrated efference copy that reflects sensory input and cortical state.

Beyond the fast AP onsets, the gating mechanism will also impact how L5PTs integrate and transform recurrent IC and top-down CC inputs into AP output. Somatic APs back-propagate into the apical dendrites, triggering the activation of calcium channels that widen the L5PTs' time window for synaptic integration (Hay and Segev, 2015). The bAPs will therefore switch the dendrites of L5PTs into an active state, and the gating mechanism assures that this switch occurs near simultaneously with responses in layer 4 that are driven directly by the thalamus. The two TC input strata could hence complement each other, ensuring that L5PTs reliably transform inputs from recurrent IC circuits—e.g., those from layers 2/3 that are driven by layer 4—into cortical output (Figure S5). This theory is in line with recent observations in L5PTs during whisker-guided behaviors, which showed that sensory-evoked Ca^{2+} transients in apical dendrites correlate with perceptual thresholds (Takahashi et al., 2016) and that active dendritic integration contributes to the transformation of sensory information into motor commands (Ranganathan et al., 2018). It also provides a potential explanation for the origin of target-related AP responses that persist for the duration of the stimulus (Rojas-Piloni et al., 2017).

Gating of cortical output via a deep TC input stratum is likely to generalize to other sensory systems and species. In macaque primary visual cortex (V1), neurons—sometimes referred to as Meynert cells—have been described whose features are reminiscent of those that characterize L6CCs in rodents: they cluster around the layer 5/6 border (Lund, 1988) and have extensive horizontal axons in the deep layers that unspecifically span across several ocular dominance columns of both the left and right eye (Li et al., 2003). Because of strong similarities in RF shapes between neurons in layers 4 and 6, it was suggested that Meynert cells might be strategically placed to receive strong TC input from the deep-layer terminal fields of lateral geniculate nucleus (LGN) axons (Lund, 1988). It was even speculated that strong TC input to horizontally projecting neurons in the deep layers represents an organizational principle that is unique to primates and which may underlie their superior cognitive capabilities (Briggs, 2010). However, bistratified LGN axons, as well as horizontally projecting L6CCs, were also reported for V1 in cats (Antonini and Stryker, 1993; Karube et al., 2017) and mice (Vélez-Fort et al., 2014).

L6CCs will be involved in other functions, beyond gating cortical output patterns. Their axons innervate all layers of vS1 but in particular layer 4. The fast and reliable activation of these neurons may therefore contribute to the substantial IC component of sensory-evoked PSPs in the major thalamorecipient layer (Cohen-Kashi Malina et al., 2016). Moreover, at least a subset of the L6CCs display long-range intrinsic axons that innervate higher-order cortices (Zhang and Deschênes, 1997), a property that they share also with the Meynert cells (Fries et al., 1985). Coordinating the onsets of activity patterns within and across cortical and subcortical circuits, horizontally projecting neurons that form a deep TC input stratum may therefore be a general feature of the neocortex.

STAR★METHODS

Detailed methods are provided in the online version of this paper and include the following:

- KEY RESOURCES TABLE
- LEAD CONTACT AND MATERIALS AVAILABILITY
- EXPERIMENTAL MODEL AND SUBJECT DETAILS
- METHOD DETAILS
  - Virus injection
  - Cell-attached recording/labeling in virus injected animals
  - Pharmacological manipulation
  - Extracellular recordings
  - Histology
  - Morphological reconstruction
  - Cell type-specific analysis
  - Multi-compartmental model
  - Connectivity model
  - Synapse models
  - Synaptic input patterns
  - Simulations
- QUANTIFICATION AND STATISTICAL ANALYSIS
- DATA AND CODE AVAILABILITY

SUPPLEMENTAL INFORMATION

Supplemental Information can be found online at https://doi.org/10.1016/j.neuron.2019.10.011.

ACKNOWLEDGMENTS

We thank Bert Sakmann for discussions; Etay Hay and Idan Segev for providing biophysical models and optimization routines; Martin Schwarz for providing the AAV; and David Fitzpatrick, Kevan Martin, and Randy Bruno for comments on the manuscript. Funding was provided from the Center of Advanced European Studies and Research, the Max Planck Institute for Biological Cybernetics, the Center for Neurogenomics and Cognitive Research, the Max Planck Institute of Neurobiology, the European Research Council under the European Union's Horizon 2020 research and innovation program (grant agreement 633428; to M.O.), the German Federal Ministry of Education and Research (grants BMBF/FKZ 01GQ1002 and 01IS18052; to M.O.), the Deutsche Forschungsgemeinschaft (SFB 1089; to M.O.), and the Studienstiftung des Deutschen Volkes (to R.E. and A.B.).

AUTHOR CONTRIBUTIONS

M.O. conceived and designed the study. R.E. developed the model and performed simulations. R.T.N. performed cell-attached recordings and pharmacology experiments. J.M.G. performed virus injections and cell-attached recordings. A.B. performed simulations. D.U. developed analysis routines. L.F.M. performed pharmacology experiments. S.D. performed extracellular recordings. C.P.J.d.K. performed cell-attached and extracellular recordings. All authors analyzed data. M.O. wrote the paper.

DECLARATION OF INTERESTS

The authors declare no competing interests.

Received: February 7, 2019
Revised: September 1, 2019
Accepted: October 2, 2019
Published: November 26, 2019

REFERENCES

Antonini, A., and Stryker, M.P. (1993). Rapid remodeling of axonal arbors in the visual cortex. Science *260*, 1819–1821.

Armstrong-James, M., and Fox, K. (1987). Spatiotemporal convergence and divergence in the rat S1 "barrel" cortex. J. Comp. Neurol. *263*, 265–281.

Arzt, M., Sakmann, B., and Meyer, H.S. (2018). Anatomical correlates of local, translaminar, and transcolumnar inhibition by layer 6 GABAergic interneurons in somatosensory cortex. Cereb. Cortex *28*, 2763–2774.

Audette, N.J., Urban-Ciecko, J., Matsushita, M., and Barth, A.L. (2018). POm thalamocortical input drives layer-specific microcircuits in somatosensory cortex. Cereb. Cortex *28*, 1312–1328.

Barthó, P., Hirase, H., Monconduit, L., Zugaro, M., Harris, K.D., and Buzsáki, G. (2004). Characterization of neocortical principal cells and interneurons by network interactions and extracellular features. J. Neurophysiol. *92*, 600–608.

Boudewijns, Z.S., Groen, M.R., Lodder, B., McMaster, M.T., Kalogreades, L., de Haan, R., Narayanan, R.T., Meredith, R.M., Mansvelder, H.D., and de Kock, C.P. (2013). Layer-specific high-frequency action potential spiking in the prefrontal cortex of awake rats. Front. Cell. Neurosci. *7*, 99.

Brecht, M., and Sakmann, B. (2002). Whisker maps of neuronal subclasses of the rat ventral posterior medial thalamus, identified by whole-cell voltage recording and morphological reconstruction. J. Physiol. *538*, 495–515.

Brecht, M., Roth, A., and Sakmann, B. (2003). Dynamic receptive fields of reconstructed pyramidal cells in layers 3 and 2 of rat somatosensory barrel cortex. J. Physiol. *553*, 243–265.

Briggs, F. (2010). Organizing principles of cortical layer 6. Front. Neural Circuits *4*, 3.

Brown, S.P., and Hestrin, S. (2009). Intracortical circuits of pyramidal neurons reflect their long-range axonal targets. Nature *457*, 1133–1136.

Brown, A.P.Y., Cossell, L., and Margrie, T.W. (2019). Visual experience regulates the intrinsic excitability of visual cortical neurons to maintain sensory function. Cell Rep. *27*, 685–689, e4.

Bruno, R.M., and Simons, D.J. (2002). Feedforward mechanisms of excitatory and inhibitory cortical receptive fields. J. Neurosci. *22*, 10966–10975.

Carvell, G.E., and Simons, D.J. (1988). Membrane potential changes in rat SmI cortical neurons evoked by controlled stimulation of mystacial vibrissae. Brain Res. *448*, 186–191.

Clack, N.G., O'Connor, D.H., Huber, D., Petreanu, L., Hires, A., Peron, S., Svoboda, K., and Myers, E.W. (2012). Automated tracking of whiskers in videos of head fixed rodents. PLoS Comput. Biol. *8*, e1002591.

Cohen-Kashi Malina, K., Mohar, B., Rappaport, A.N., and Lampl, I. (2016). Local and thalamic origins of correlated ongoing and sensory-evoked cortical activities. Nat. Commun. *7*, 12740.

Constantinople, C.M., and Bruno, R.M. (2013). Deep cortical layers are activated directly by thalamus. Science *340*, 1591–1594.

Crandall, S.R., Patrick, S.L., Cruikshank, S.J., and Connors, B.W. (2017). Infrabarrels are layer 6 circuit modules in the barrel cortex that link long-range inputs and outputs. Cell Rep. *21*, 3065–3078.

de Kock, C.P., Bruno, R.M., Spors, H., and Sakmann, B. (2007). Layer- and cell-type-specific suprathreshold stimulus representation in rat primary somatosensory cortex. J. Physiol. *581*, 139–154.

Dercksen, V.J., Hege, H.C., and Oberlaender, M. (2014). The Filament Editor: an interactive software environment for visualization, proof-editing and analysis of 3D neuron morphology. Neuroinformatics *12*, 325–339.

Druckmann, S., Banitt, Y., Gidon, A., Schürmann, F., Markram, H., and Segev, I. (2007). A novel multiple objective optimization framework for constraining conductance-based neuron models by experimental data. Front. Neurosci. *1*, 7–18.

Economo, M.N., Viswanathan, S., Tasic, B., Bas, E., Winnubst, J., Menon, V., Graybuck, L.T., Nguyen, T.N., Smith, K.A., Yao, Z., et al. (2018). Distinct descending motor cortex pathways and their roles in movement. Nature *563*, 79–84.

Egger, R., Narayanan, R.T., Helmstaedter, M., de Kock, C.P., and Oberlaender, M. (2012). 3D reconstruction and standardization of the rat vibrissal cortex for precise registration of single neuron morphology. PLoS Comput. Biol. *8*, e1002837.

Egger, R., Dercksen, V.J., Udvary, D., Hege, H.C., and Oberlaender, M. (2014). Generation of dense statistical connectomes from sparse morphological data. Front. Neuroanat. *8*, 129.

Egger, R., Schmitt, A.C., Wallace, D.J., Sakmann, B., Oberlaender, M., and Kerr, J.N. (2015). Robustness of sensory-evoked excitation is increased by inhibitory inputs to distal apical tuft dendrites. Proc. Natl. Acad. Sci. USA *112*, 14072–14077.

Feldmeyer, D., Lübke, J., Silver, R.A., and Sakmann, B. (2002). Synaptic connections between layer 4 spiny neurone-layer 2/3 pyramidal cell pairs in juvenile rat barrel cortex: physiology and anatomy of interlaminar signalling within a cortical column. J. Physiol. *538*, 803–822.

Feldmeyer, D., Brecht, M., Helmchen, F., Petersen, C.C., Poulet, J.F., Staiger, J.F., Luhmann, H.J., and Schwarz, C. (2013). Barrel cortex function. Prog. Neurobiol. *103*, 3–27.

Fox, K., Wright, N., Wallace, H., and Glazewski, S. (2003). The origin of cortical surround receptive fields studied in the barrel cortex. J. Neurosci. *23*, 8380–8391.

Fries, W., Keizer, K., and Kuypers, H.G. (1985). Large layer VI cells in macaque striate cortex (Meynert cells) project to both superior colliculus and prestriate visual area V5. Exp. Brain Res. *58*, 613–616.

Guo, C., Peng, J., Zhang, Y., Li, A., Li, Y., Yuan, J., Xu, X., Ren, M., Gong, H., and Chen, S. (2017). Single-axon level morphological analysis of corticofugal projection neurons in mouse barrel field. Sci. Rep. *7*, 2846.

Gupta, A., Wang, Y., and Markram, H. (2000). Organizing principles for a diversity of GABAergic interneurons and synapses in the neocortex. Science *287*, 273–278.

Harris, K.D., and Shepherd, G.M. (2015). The neocortical circuit: themes and variations. Nat. Neurosci. *18*, 170–181.

Hay, E., and Segev, I. (2015). Dendritic excitability and gain control in recurrent cortical microcircuits. Cereb. Cortex *25*, 3561–3571.

Hay, E., Hill, S., Schürmann, F., Markram, H., and Segev, I. (2011). Models of neocortical layer 5b pyramidal cells capturing a wide range of dendritic and perisomatic active properties. PLoS Comput. Biol. *7*, e1002107.

Hay, E., Schürmann, F., Markram, H., and Segev, I. (2013). Preserving axosomatic spiking features despite diverse dendritic morphology. J. Neurophysiol. *109*, 2972–2981.

Helmstaedter, M., Sakmann, B., and Feldmeyer, D. (2009). L2/3 interneuron groups defined by multiparameter analysis of axonal projection, dendritic geometry, and electrical excitability. Cereb. Cortex *19*, 951–962.

Hines, M.L., and Carnevale, N.T. (1997). The NEURON simulation environment. Neural Comput. *9*, 1179–1209.

Horikawa, K., and Armstrong, W.E. (1988). A versatile means of intracellular labeling: injection of biocytin and its detection with avidin conjugates. J. Neurosci. Methods *25*, 1–11.

Ito, M. (1992). Simultaneous visualization of cortical barrels and horseradish peroxidase-injected layer 5b vibrissa neurones in the rat. J. Physiol. *454*, 247–265.

Jahr, C.E., and Stevens, C.F. (1990). A quantitative description of NMDA receptor-channel kinetic behavior. J. Neurosci. *10*, 1830–1837.

Jiang, X., Shen, S., Cadwell, C.R., Berens, P., Sinz, F., Ecker, A.S., Patel, S., and Tolias, A.S. (2015). Principles of connectivity among morphologically defined cell types in adult neocortex. Science *350*, aac9462.

Karube, F., Sári, K., and Kisvárday, Z.F. (2017). Axon topography of layer 6 spiny cells to orientation map in the primary visual cortex of the cat (area 18). Brain Struct. Funct. *222*, 1401–1426.

Koelbl, C., Helmstaedter, M., Lübke, J., and Feldmeyer, D. (2015). A barrel-related interneuron in layer 4 of rat somatosensory cortex with a high intrabarrel connectivity. Cereb. Cortex *25*, 713–725.

Kumar, P., and Ohana, O. (2008). Inter- and intralaminar subcircuits of excitatory and inhibitory neurons in layer 6a of the rat barrel cortex. J. Neurophysiol. *100*, 1909–1922.

Kwegyir-Afful, E.E., Bruno, R.M., Simons, D.J., and Keller, A. (2005). The role of thalamic inputs in surround receptive fields of barrel neurons. J. Neurosci. *25*, 5926–5934.

Larkum, M.E., Kaiser, K.M., and Sakmann, B. (1999a). Calcium electrogenesis in distal apical dendrites of layer 5 pyramidal cells at a critical frequency of back-propagating action potentials. Proc. Natl. Acad. Sci. USA *96*, 14600–14604.

Larkum, M.E., Zhu, J.J., and Sakmann, B. (1999b). A new cellular mechanism for coupling inputs arriving at different cortical layers. Nature *398*, 338–341.

Larkum, M.E., Nevian, T., Sandler, M., Polsky, A., and Schiller, J. (2009). Synaptic integration in tuft dendrites of layer 5 pyramidal neurons: a new unifying principle. Science *325*, 756–760.

Lee, S., Carvell, G.E., and Simons, D.J. (2008). Motor modulation of afferent somatosensory circuits. Nat. Neurosci. *11*, 1430–1438.

Lee, J.H., Shin, H.S., Lee, K.H., and Chung, S. (2015). LFP-guided targeting of a cortical barrel column for in vivo two-photon calcium imaging. Sci. Rep. *5*, 15905.

Lefort, S., Tomm, C., Floyd Sarria, J.C., and Petersen, C.C. (2009). The excitatory neuronal network of the C2 barrel column in mouse primary somatosensory cortex. Neuron *61*, 301–316.

Li, H., Fukuda, M., Tanifuji, M., and Rockland, K.S. (2003). Intrinsic collaterals of layer 6 Meynert cells and functional columns in primate V1. Neuroscience *120*, 1061–1069.

Lund, J.S. (1988). Anatomical organization of macaque monkey striate visual cortex. Annu. Rev. Neurosci. *11*, 253–288.

Manns, I.D., Sakmann, B., and Brecht, M. (2004). Sub- and suprathreshold receptive field properties of pyramidal neurones in layers 5A and 5B of rat somatosensory barrel cortex. J. Physiol. *556*, 601–622.

Mao, T., Kusefoglu, D., Hooks, B.M., Huber, D., Petreanu, L., and Svoboda, K. (2011). Long-range neuronal circuits underlying the interaction between sensory and motor cortex. Neuron *72*, 111–123.

Meye, F.J., Soiza-Reilly, M., Smit, T., Diana, M.A., Schwarz, M.K., and Mameli, M. (2016). Shifted pallidal co-release of GABA and glutamate in habenula drives cocaine withdrawal and relapse. Nat. Neurosci. *19*, 1019–1024.

Meyer, H.S., Egger, R., Guest, J.M., Foerster, R., Reissl, S., and Oberlaender, M. (2013). Cellular organization of cortical barrel columns is whisker-specific. Proc. Natl. Acad. Sci. USA *110*, 19113–19118.

Narayanan, R.T., Mohan, H., Broersen, R., de Haan, R., Pieneman, A.W., and de Kock, C.P. (2014). Juxtasomal biocytin labeling to study the structure-function relationship of individual cortical neurons. J. Vis. Exp. e51359.

Narayanan, R.T., Egger, R., Johnson, A.S., Mansvelder, H.D., Sakmann, B., de Kock, C.P., and Oberlaender, M. (2015). Beyond columnar organization: cell type- and target layer-specific principles of horizontal axon projection patterns in rat vibrissal cortex. Cereb. Cortex *25*, 4450–4468.

Narayanan, R.T., Udvary, D., and Oberlaender, M. (2017). Cell type-specific structural organization of the six layers in rat barrel cortex. Front. Neuroanat. *11*, 91.

Oberlaender, M., Bruno, R.M., Sakmann, B., and Broser, P.J. (2007). Transmitted light brightfield mosaic microscopy for three-dimensional tracing of single neuron morphology. J. Biomed. Opt. *12*, 064029.

Oberlaender, M., de Kock, C.P., Bruno, R.M., Ramirez, A., Meyer, H.S., Dercksen, V.J., Helmstaedter, M., and Sakmann, B. (2012a). Cell type-specific three-dimensional structure of thalamocortical circuits in a column of rat vibrissal cortex. Cereb. Cortex *22*, 2375–2391.

Oberlaender, M., Ramirez, A., and Bruno, R.M. (2012b). Sensory experience restructures thalamocortical axons during adulthood. Neuron *74*, 648–655.

Perin, R., Berger, T.K., and Markram, H. (2011). A synaptic organizing principle for cortical neuronal groups. Proc. Natl. Acad. Sci. USA *108*, 5419–5424.

Petersen, C.C., Hahn, T.T., Mehta, M., Grinvald, A., and Sakmann, B. (2003). Interaction of sensory responses with spontaneous depolarization in layer 2/3 barrel cortex. Proc. Natl. Acad. Sci. USA *100*, 13638–13643.

Petreanu, L., Mao, T., Sternson, S.M., and Svoboda, K. (2009). The subcellular organization of neocortical excitatory connections. Nature *457*, 1142–1145.

Ramaswamy, S., and Markram, H. (2015). Anatomy and physiology of the thick-tufted layer 5 pyramidal neuron. Front. Cell. Neurosci. *9*, 233.

Ramirez, A., Pnevmatikakis, E.A., Merel, J., Paninski, L., Miller, K.D., and Bruno, R.M. (2014). Spatiotemporal receptive fields of barrel cortex revealed by reverse correlation of synaptic input. Nat. Neurosci. *17*, 866–875.

Ranganathan, G.N., Apostolides, P.F., Harnett, M.T., Xu, N.L., Druckmann, S., and Magee, J.C. (2018). Active dendritic integration and mixed neocortical network representations during an adaptive sensing behavior. Nat. Neurosci. *21*, 1583–1590.

Reyes-Puerta, V., Sun, J.J., Kim, S., Kilb, W., and Luhmann, H.J. (2015). Laminar and columnar structure of sensory-evoked multineuronal spike sequences in adult rat barrel cortex in vivo. Cereb. Cortex *25*, 2001–2021.

Rojas-Piloni, G., Guest, J.M., Egger, R., Johnson, A.S., Sakmann, B., and Oberlaender, M. (2017). Relationships between structure, in vivo function and long-range axonal target of cortical pyramidal tract neurons. Nat. Commun. *8*, 870.

Rossant, C., Kadir, S.N., Goodman, D.F.M., Schulman, J., Hunter, M.L.D., Saleem, A.B., Grosmark, A., Belluscio, M., Denfield, G.H., Ecker, A.S., et al. (2016). Spike sorting for large, dense electrode arrays. Nat. Neurosci. *19*, 634–641.

Salami, M., Itami, C., Tsumoto, T., and Kimura, F. (2003). Change of conduction velocity by regional myelination yields constant latency irrespective of distance between thalamus and cortex. Proc. Natl. Acad. Sci. USA *100*, 6174–6179.

Schnepel, P., Kumar, A., Zohar, M., Aertsen, A., and Boucsein, C. (2015). Physiology and impact of horizontal connections in rat neocortex. Cereb. Cortex *25*, 3818–3835.

Schoonover, C.E., Tapia, J.C., Schilling, V.C., Wimmer, V., Blazeski, R., Zhang, W., Mason, C.A., and Bruno, R.M. (2014). Comparative strength and dendritic organization of thalamocortical and corticocortical synapses onto excitatory layer 4 neurons. J. Neurosci. *34*, 6746–6758.

Siegle, J.H., López, A.C., Patel, Y.A., Abramov, K., Ohayon, S., and Voigts, J. (2017). Open Ephys: an open-source, plugin-based platform for multichannel electrophysiology. J. Neural Eng. *14*, 045003.

Song, S., Sjöström, P.J., Reigl, M., Nelson, S., and Chklovskii, D.B. (2005). Highly nonrandom features of synaptic connectivity in local cortical circuits. PLoS Biol. *3*, e68.

Takahashi, N., Oertner, T.G., Hegemann, P., and Larkum, M.E. (2016). Active cortical dendrites modulate perception. Science *354*, 1587–1590.

Thomson, A.M., West, D.C., Hahn, J., and Deuchars, J. (1996). Single axon IPSPs elicited in pyramidal cells by three classes of interneurones in slices of rat neocortex. J. Physiol. *496*, 81–102.

Thomson, A.M., West, D.C., Wang, Y., and Bannister, A.P. (2002). Synaptic connections and small circuits involving excitatory and inhibitory neurons in layers 2-5 of adult rat and cat neocortex: triple intracellular recordings and biocytin labelling in vitro. Cereb. Cortex *12*, 936–953.

Varga, Z., Jia, H., Sakmann, B., and Konnerth, A. (2011). Dendritic coding of multiple sensory inputs in single cortical neurons in vivo. Proc. Natl. Acad. Sci. USA *108*, 15420–15425.

Vélez-Fort, M., Rousseau, C.V., Niedworok, C.J., Wickersham, I.R., Rancz, E.A., Brown, A.P., Strom, M., and Margrie, T.W. (2014). The stimulus selectivity and connectivity of layer six principal cells reveals cortical microcircuits underlying visual processing. Neuron *83*, 1431–1443.

Viaene, A.N., Petrof, I., and Sherman, S.M. (2011). Properties of the thalamic projection from the posterior medial nucleus to primary and secondary somatosensory cortices in the mouse. Proc. Natl. Acad. Sci. USA *108*, 18156–18161.

Wimmer, V.C., Bruno, R.M., de Kock, C.P., Kuner, T., and Sakmann, B. (2010). Dimensions of a projection column and architecture of VPM and POm axons in rat vibrissal cortex. Cereb. Cortex *20*, 2265–2276.

Wong-Riley, M. (1979). Changes in the visual system of monocularly sutured or enucleated cats demonstrable with cytochrome oxidase histochemistry. Brain Res. *171*, 11–28.

Wozny, C., and Williams, S.R. (2011). Specificity of synaptic connectivity between layer 1 inhibitory interneurons and layer 2/3 pyramidal neurons in the rat neocortex. Cereb. Cortex *21*, 1818–1826.

Wright, N., and Fox, K. (2010). Origins of cortical layer V surround receptive fields in the rat barrel cortex. J. Neurophysiol. *103*, 709–724.

Zhang, Z.W., and Deschênes, M. (1997). Intracortical axonal projections of lamina VI cells of the primary somatosensory cortex in the rat: a single-cell labeling study. J. Neurosci. *17*, 6365–6379.

STAR★METHODS

KEY RESOURCES TABLE

REAGENT or RESOURCE	SOURCE	IDENTIFIER
Antibodies		
Rabbit anti-mCherry	Invitrogen	Cat#PA5-34974; RRID: AB_2552323
Rat anti-mCherry	Invitrogen	Cat#M11217; RRID: AB_2536611
Mouse anti-Vglut2	Chemicon	Cat#MAB5504; RRID: AB_2187552
Rabbit anti-VGlut2	Synaptic Systems	Cat#135403; RRID: AB_887883
Goat anti-Rabbit IgG Alexa-647 H^+L	Invitrogen	Cat#A21245; RRID: AB_2535813
Goat-anti-Mouse IgG Alexa 405 H^+L	Invitrogen	Cat#A31553; RRID: AB_221604
Goat anti-Rabbit IgG Alexa 488 H^+L	Invitrogen	Cat#A11034; RRID: AB_2576217
Goat anti-Rat IgG Alexa 647 H^+L	Invitrogen	Cat#A21247; RRID: AB_141778
Bacterial and Virus Strains		
rAAV2/1-CAG-hChR2(H134R)-Syn-mCherry	Meye et al., 2016	Martin Schwarz, University of Bonn Medical Center, Lot #128
Biological Samples		
Normal Goat Serum	Jackson ImmunoResearch	Cat#005-000-121; RRID: AB_2336990
Chemicals, Peptides, and Recombinant Proteins		
Streptavidin, Alexa 488 Conjugate	Invitrogen	Cat#S11223
Biocytin	Sigma Aldrich	B4261; CAS 576-19-2
Cytochrome C from equine heart	Sigma Aldrich	C2506; CAS 9007-43-6
Catalase from bovine liver	Sigma Aldrich	C9322; CAS 9001-05-2
DAB	Sigma Aldrich	D5637; CAS 868272-85-9
Muscimol	Sigma Aldrich	M1523; CAS 2763-96-4
Triton x100	Sigma Aldrich	T9284; CAS 9002-93-1
Hydrogen Peroxide Solution	Sigma Aldrich	CAS 7722-84-1
Critical Commercial Assays		
Vectastain ABC kit	Vector	Cat#PK-6100; RRID: AB_2336819
Experimental Models: Organisms/Strains		
Wistar rats (Rattus norvegicus)	Charles River	Crl:WI
Software and Algorithms		
Amira	FEI	version 5
FilamentEditor (Amira plugin)	Dercksen et al., 2014	http://www.zib.de/software/neuron-reconstruction
NeuroMorph neuron morphology reconstruction	Oberlaender et al., 2007	N/A
NeuroNet (Amira plugin)	Egger et al., 2014	http://www.zib.de/software/neuronet
R software package	https://www.r-project.org	version 3.4.3
scipy	https://www.scipy.org	version 1.0.1
NEURON	Hines and Carnevale, 1997	https://www.neuron.yale.edu/neuron/
L5PT neuron model	This paper	https://senselab.med.yale.edu/modeldb/ShowModel.cshtml?model=239145
Klustakwik	Rossant et al., 2016	https://github.com/kwikteam/klusta
Spike2	Cambridge Electronic Design	Version 9
Other		
Intracellular microelectrode recording amplifier	Axon Instruments	Axoclamp 2B
Extracellular microelectrode recording amplifier	npi electronic GmbH	ELC-01X
Data acquisition board	Cambridge Electronic Design	CED power1401
Multi-channel silicon probe	Atlas Neuroengineering	E32+R-50-S1-L10(NT)

(*Continued on next page*)

Continued

REAGENT or RESOURCE	SOURCE	IDENTIFIER
Extracellular multi-channel electrode recording amplifier	Intan Technologies	RHD2132
Data acquisition board	Open Ephys	http://www.open-ephys.org/acq-board/
SlowFade Gold embedding medium	Invitrogen	Cat#S36936
Brightfield microscope	Olympus	BX-51
Confocal laser scanning microscope	Leica Microsystems	Leica Application Suite Advanced Fluorescence SP5
Confocal laser scanning super resolution microscope	Leica Microsystems	Leica Application Suite X Navigator Lightning SP8
LED (470 nm)	Thorlabs	Cat#M470F3
Optical fiber	Thorlabs	Cat#RJPSF2
High-speed infrared camera	IDT Europe	MotionScope M3

LEAD CONTACT AND MATERIALS AVAILABILITY

Further information and requests for resources and reagents should be directed to and will be fulfilled by the Lead Contact, Marcel Oberlaender (marcel.oberlaender@caesar.de). This study did not generate new unique reagents.

EXPERIMENTAL MODEL AND SUBJECT DETAILS

For *in vivo* animal studies, Male Wistar rats aged 22-70 days (P22-70, m) were provided by Charles River Laboratories. All experiments were carried out after evaluation by the local German authorities, in accordance with the animal welfare guidelines of the Max Planck Society, or with the Dutch law after evaluation by a local ethical committee at the VU University Amsterdam, the Netherlands.

METHOD DETAILS

Virus injection

Wistar rats (P22-25, m) were anesthetized with isoflurane supplemented by rimadyl (Caprofen, 5mg/ kg) as analgesia, then placed into a stereotaxic frame (Kopf Instruments, model 1900), and provided with a continuous flow of isoflurane/O_2 gas. Body temperature was maintained at 37°C by a heating pad. A small craniotomy was made above the left hemisphere 2.85 mm posterior to bregma and 3.2 mm lateral from the midline. The head of the rat was leveled with a precision of 1 μm in both the medial-lateral and anterior-posterior planes using an eLeVeLeR electronic leveling device (Sigmann Electronics, Hüffenhardt, Germany) mounted to an adaptor of the stereotaxic frame. An injecting pipette containing an adeno-associated virus (AAV) was lowered into the VPM thalamus (5.05 mm from the pia). The virus (Meye et al., 2016) – rAAV2/1-CAG-hChR2(H134R)-Syn-mCherry (titer: $1x10^{12}$ gc ml^{-1}) – was provided by Martin Schwarz (University of Bonn, Germany). 50-70 nL of the virus were injected using a 30cc syringe coupled to a calibrated glass injection capillary.

Cell-attached recording/labeling in virus injected animals

After a 16-21 day incubation period, AAV injected rats were anesthetized with urethane (1.8 g/kg body weight) by intraperitoneal injection. The depth of anesthesia was assessed by monitoring pinch withdrawal, eyelid reflexes, and vibrissae movements. Body temperature was maintained at 37.5 ± 0.5°C by a heating pad. Cell-attached recording and labeling was performed as described in detail previously (Narayanan et al., 2014). Briefly, APs were recorded using an extracellular loose patch amplifier (ELC-01X, npi electronic GmbH), and digitized using a CED power1401 data acquisition board (CED, Cambridge Electronic Design, Cambridge, UK). APs were recorded before and during 20-30 trials of caudal multi-whisker deflections by a 700 ms airpuff (10 PSI), delivered through a 1 mm plastic tube from a distance of 8-10 cm from the whisker pad (Rojas-Piloni et al., 2017). Stimulation was repeated at constant intervals (0.3 Hz). Optical stimulation of ChR2-expressing thalamocortical terminals was provided by a 200 μm diameter optical fiber (ThorLabs #RJPSF2) coupled to a 470 nm wavelength LED (ThorLabs M470F3), resulting in an output power of 1 mW. The fiber was positioned approximately 2 mm above the cortical surface, resulting in a 1-2 mm disc of light above vS1. APs were recorded during 20-30 trials of 10 ms light pulses, at an inter-stimulus interval of 2.5 s. Following the electrophysiological measurements, neurons were filled with biocytin. Filling sessions were repeated several times. After 1-2 hours for tracer diffusion, animals were transcardially perfused with 0.9% saline followed by 4% paraformaldehyde (PFA). Brains were removed and post-fixed with 4% PFA for 24 hours, transferred to 0.05 M phosphate buffer (PB) and stored at 4°C.

Pharmacological manipulation

Wistar rats (P28-P35, m) were anesthetized with urethane (1.6-1.7 g/kg body weight) by intraperitoneal injection. As described above, the depth of anesthesia was monitored, and the animal's body temperature was maintained. An 'L' shaped craniotomy centered on the coordinate of the barrel column representing the D2 whisker (2.5 mm posterior and 5.5 mm lateral to the bregma) was made without cutting the dura, and extended along the rostro-medial (i.e., along the E-row) and caudal axes (i.e., arc 2) for ~1-2 mm, respectively. Locations for muscimol injections and recordings were determined with long-tapered 'search pipettes' (tip diameter < 3 μm and insertion diameter < 50μm). The search pipette was inserted rostral to vS1 and lowered parallel to the midline while measuring LFPs at different cortical depths, and in response to deflections of different individual whiskers using a piezoelectric bimorph (Lee et al., 2015). Recordings were made using an Axoclamp 2B amplifier (Axon instruments, Union City, CA, USA), low pass filtered (300 Hz), and digitized using a CED power1401 data acquisition board (CED, Cambridge Electronic Design, Cambridge, UK). Using the LFP data, we identified the depth of the L5/6 border and the PW (e.g., E2), and marked this location on the dura with a surgical pen. Repeating the LFP-guided whisker mapping with a second search pipette that was inserted approximately parallel to the vertical axis of vS1, we identified layer 5 of the hence appropriate recording site (i.e., C2 if the PW at the injection site was E2). This location was also marked on the dura. Pipettes for muscimol injections were prepared with a tip diameter of 8-12 μm followed by beveling of the tip. The taper diameter at the insertion point into the brain was ~125-150 μm. The tip of the pipette was filled with normal rat ringer (NRR) to avoid muscimol spill upon pipette insertion. The rest of the pipette was filled with 10 mM muscimol supplemented with 2% biocytin. The injection pipette was positioned at the previously determined location, the dura was cut open (~500 μm), and the injection pipette was inserted with positive pressure of 5-10 mbar. Allowing the tissue to adjust for 10-15 minutes, we inserted a recording pipette (i.e., 1 μm tip diameter, filled with NRR supplemented with 2% biocytin) at the second previously determined location. Both locations were confirmed by measuring whisker-evoked LFPs. L5PTs were identified as follows (de Kock et al., 2007; Manns et al., 2004; Oberlaender et al., 2012a): (1) recording depth between 1000-1600 μm; (2) ongoing AP rates between ~1-5 Hz; (3) reliable and fast APs (i.e., between 10-20 ms) in response to PW deflections; (4) reliable and fast APs after deflection of the manipulated whisker. We identified eight neurons that matched these criteria (recording / injection location: 1x B1/D1, 4x C1/E1, 3x C2/E2). Whisker deflections of the PW at the recording site (e.g., C2), the intermediate SW (e.g., D2) and the manipulated 2nd SW (e.g., E2) were performed (i.e., 50 trials of 200 ms ramp-and-hold stimulus with an amplitude of ~5°, 2 s inter-stimulus interval), and APs were recorded, while simultaneously measuring LFPs via the injection pipette. Following these measurements (i.e., control data), muscimol was injected by slowly increasing the pressure onto the injection pipette (80-300 mbar), while monitoring the LFP in response to deflections of the manipulated 2nd SW. Once 2nd SW-evoked LFPs were abolished at the injection site, and ongoing AP activity at the recording site remained unaffected, the measurements of whisker-evoked responses were repeated (i.e., at least 50 trials of PW, SW and 2nd SW deflections, respectively). In additional control experiments, the injection pipettes were positioned either at the border between layers 2 and 3 (i.e., recording depth of 290 ± 55 μm, n = 5) or close to the white matter in deep layer 6 (1,841 ± 76 μm, n = 3). L5PTs were targeted as before. The spatial extent of the functional effect by muscimol injections was measured by placing injection pipettes at the L5/6 border, and recording LFPs via the injection pipette in response to deflections of the whisker that was somatotopically aligned with the injection site (i.e., manipulated PW) and one SW before and after muscimol injections. Once LFP responses to PW deflections were abolished, injection pipettes were retracted in 50 or 100 μm steps (up to 900 μm from the injection site) along the whisker arc toward layer 4 of the barrel column that represented the deflected SW, and LFP responses were measured at each location. This procedure was repeated multiple times.

Extracellular recordings

Wistar rats (P33-P70, m) were anesthetized using 1.6% isoflurane in 0.4 l/h O_2 + 0.7 l/h NO_2, supplemented by rimadyl (Caprofen, 5mg/ kg) as analgesia. A craniotomy of 0.5 mm x 0.5 mm was made above vS1 on the left hemisphere, and a head post for fixation was implanted on the skull. After recovery from surgery, rats were head-fixed two times per day for 2-3 days. Rats quickly adjusted to the head-fixation, allowing stable recording conditions without the need of body restraint. Rats were anaesthetized with isoflurane (1.25% in 0.4 l/h O_2 + 0.7 l/h NO_2), and a 32-channel linear silicon probe (E32+R-50-S1-L10(NT), Atlas Neuroengineering, Belgium) was inserted into vS1 for extracellular multi-unit recordings. Prior to recordings, silicon probes were labeled with DiI (Thermo Fisher Scientific, Waltham, MA, USA). The probe was connected to a unity-gain headstage (Neuralynx, USA), in series with the Open Ephys data acquisition board equipped with a RHD2132 digital interface chip (Intan Technologies, Los Angeles, CA, USA). Using the LFP strategy described above, the PW at the recording site was identified, all other whiskers were trimmed to 5 mm, and the anesthesia was terminated. Recordings were performed once the animals were fully awake (~25 minutes after the anesthesia was terminated (Boudewijns et al., 2013)). Rats were not trained to perform tactile behavior, and behavior was not rewarded. Sensory input resulted from whisker touch with a pole that was placed within range during periods of exploratory whisker self-motion. The touch onset was determined by high-speed videography at 200 frames/s (MotionScope M3 camera, IDT Europe, Belgium). Whisker angle was tracked offline (Clack et al., 2012), and episodes of whisker movements were classified by thresholding average power in whisker angle versus time (1-20 Hz bandpass) using the MATLAB spectrogram function. Touch events were detected manually in each frame. Signals were acquired at a sampling rate of 30 kHz/channel using Open Ephys GUI (Siegle et al., 2017). To identify single units, the data were high-pass filtered, and automatically sorted into clusters using Klustakwik (Rossant et al., 2016). The clusters were manually post-processed, and only stable and well-isolated single units were considered for analysis. The average waveforms of all well-isolated single units were used to sub-classify units (Barthó et al., 2004) as regular spiking versus fast spiking units

(FSUs). FSUs (AP peak-to-trough time < 0.5 ms and AP half-peak time < 0.25 ms) were excluded from the analyses. After recordings, rats were anaesthetized with urethane (> 2.0 g/kg) and perfused with 0.9% NaCl followed by 4% paraformaldehyde (PFA).

Histology

For morphological reconstructions, 100 μm thick vibratome sections were cut tangentially to vS1 (45° angle) ranging from the pial surface to the white matter (WM). Sections were processed for cytochrome-C oxidase staining to visualize barrel contours in layer 4 (Wong-Riley, 1979). All sections were treated with avidin-biotin (ABC) solution, and subsequently neurons were identified using the chromogen 3,3′-diaminobenzidine tetrahydrochloride (DAB) (Horikawa and Armstrong, 1988). All sections were mounted on glass slides, embedded with Mowiol, and enclosed with a coverslip. In experiments where virus injections were combined with *in vivo* recording/photo-stimulation, biocytin filling and/or quantification of primary thalamic glutamatergic synapses, cortex was cut either into 45-48 consecutive 50 μm thick tangential slices or 50 μm thick coronal slices to include vS1 and the VPM virus injection site. Sections were treated with Streptavidin Alexa 488 conjugate (5mg/ml Molecular Probes #S11223) to stain biocytin labeled morphologies (Rojas-Piloni et al., 2017). To enhance the fluorescence expressed by the virus and to label primary thalamic synapses, slices were then double immunolabeled with anti-mCherry antibody and anti-VGlut2 antibody. Sections were permeabilized and blocked in 0.5% Triton x-100 (TX) (Sigma Aldrich #9002-93-1) in 100 mM PB containing 4% normal goat serum (NGS) (Jackson ImmunoResearch Laboratories #005-000-121) for 2 hours at room temperature. The primary antibodies were diluted 1:500 (Rabbit anti-mCherry, Invitrogen #PA5-34974 and Mouse anti-Vglut2, Chemicon #MAB5504 or Rat anti-mCherry Invitrogen #M11217 and Rabbit anti-VGlut2 antibody, Synaptic Systems #135403) in PB containing 1% NGS for 48 hours at 4°C. The secondary antibodies were diluted (1:500 goat anti-Rabbit IgG Alexa-647 H^+L Invitrogen #A21245 and goat anti-Mouse IgG Alexa-405 H^+L Invitrogen #A31553 or 1:500 goat anti-Rabbit IgG Alexa-488 H^+L Invitrogen #A11034 and goat anti-Rat IgG Alexa-647 H^+L Invitrogen #A21247) and were incubated for 2-3 hours at room temperature in PB containing 3% NGS and 0.3% TX. All sections were mounted on glass slides, embedded with SlowFade Gold (Invitrogen #S36936) and enclosed with a coverslip. For extracellular recording experiments, brains were post-fixed in 4% PFA, and tangential vibratome sections (100 μm) were cut and stained for cytochrome-C. An X-Cite 120 Q light-source (Excelitas Technologies Corp., Waltham, MA, USA) was used to visualize the DiI electrode tract, and only electrode tracks within the barrel column that represents the PW were selected for analyses. The histology allowed assigning the recording depth to each electrode (i.e., and hence to each unit) with approximately 100 μm precision.

Morphological reconstruction

Neuronal structures were extracted from image stacks using a previously reported automated tracing software (Oberlaender et al., 2007). 3D image stacks of up to 5 mm × 5 mm × 0.1 mm were acquired using an automated brightfield microscope system (BX-51, Olympus, Japan) at a resolution of 0.092 × 0.092 × 0.5 μm per voxel (100 × magnification, NA 1.4). For reconstruction of fluorescently labeled neurons and AAV-based synapse mapping, images were acquired using a confocal laser scanning system (Leica Application Suite Advanced Fluorescence SP5; Leica Microsystems). 3D image stacks of up to 2.5 mm × 2.5 mm × 0.05 mm were acquired at a resolution of 0.092 × 0.092 × 0.5 μm per voxel (63 × magnification, NA 1.3). Image stacks were acquired for each of 45-48 consecutive 50 μm thick tangential brain slices that range from the pial surface to the white matter. Manual proof-editing of individual sections, and automated alignment across sections were performed using custom-designed software (Dercksen et al., 2014). Pia, barrel and WM outlines were manually drawn on low-resolution images (4 ×). Using these anatomical reference structures, all reconstructed dendrite and axon morphologies were registered to the D2 barrel column of a standardized 3D reference frame of rat vS1 (Egger et al., 2012). The shortest distance from the pial surface to the soma, and 20 morphological features that have previously been shown to separate between excitatory cell types in rat vS1 (Oberlaender et al., 2012a) were calculated for each reconstructed and registered dendrite morphology. For identification of putative TC synapses, biocytin labeled morphologies and AAV labeled VPM terminals were imaged simultaneously using the confocal laser scanning system as described above: biocytin Alexa-488 (excited at 488 nm, emission detection range 495-550 nm), AAV Alexa-647 (excited at 633 nm, emission detection range 650-785 nm). These dual-channel image stacks were loaded into Amira visualization software (FEI). All reconstructed dendrites were manually inspected, and landmarks were placed onto each spine head. If a spine head was overlapping with a VPM bouton, an additional landmark was placed to mark a putative synapse. The shortest distance of each landmark to the dendrite reconstruction was determined, and the path length distance was calculated from that location along the reconstructed L6CC to the soma. For validation of putative TC synapses, image stacks were acquired with an inverted super-resolution enhanced confocal laser scanning system (Leica Application Suite Advance Lightening Fluorescence SP8; Leica Microsystems) equipped with glycerol/oil immersion objectives (HC PL APO 10x 0.04 N.A., HC PL APO 20x 0.7 N.A., and HCX PL APO 63x 1.3 N.A.), a tandem scanning system (Resonance Scanner: 8 kHz scanning speed), spectral detectors with hybrid technology (GaAsP photocathode; 8x line average): VGlu2 Alexa-405 (excited at 405 nm, emission detection range: 410-480 nm), biocytin Alexa-488 (excited at 488 nm, emission detection range 495-550 nm), AAV Alexa-647 (excited at 633 nm, emission detection range 650-785 nm). Triple-channel image stacks of representative parts of the basal and apical dendrites of a L6CC (Figure 8) were acquired at a resolution of 29.5 × 29.5 × 130 nm per voxel (i.e., as determined by the default settings of the lightning suite). Image stacks were loaded into Amira visualization software, and manually inspected for overlap within a single optical section between spine heads and AAV- and/or VGlu2-positive VPM boutons.

Cell type-specific analysis

In total, n = 177 *in vivo* labeled morphologies of excitatory neurons in vS1 (i.e., from urethane anesthetized Wistar rats; P25-P45, m/f, Charles River) were used in this study to determine cell type-specific whisker receptive fields (wRFs), and to provide structural/functional constrains for simulation experiments. All morphologies (Narayanan et al., 2015; Rojas-Piloni et al., 2017) – except for five L6CCs and one L5PT – and classification approaches (Narayanan et al., 2015; Oberlaender et al., 2012a), as well as the corresponding whisker-evoked physiology data (de Kock et al., 2007; Oberlaender et al., 2012a) have been reported previously, but in different context. Analysis of wRFs for objectively classified morphological cell types were not performed for any of the previously reported neurons. Here, each neuron was objectively assigned to one of the 10 major excitatory cell types of the neocortex (Harris and Shepherd, 2015; Narayanan et al., 2015) based on the 21 soma-dendritic features described above: three types of pyramids in layers 2-4 (L2PY, L3PY, L4PY), spiny-stellates (L4ss) and star-pyramids in layer 4 (L4sp), slender-tufted intratelencephalic (L5IT) and thick-tufted pyramidal tract neurons in layer 5 (L5PT), corticocortical (L6CC), polymorphic corticocortical (L6INV) and corticothalamic neurons in layer 6 (L6CT). In the present study, we grouped L4ss and L4sp as layer 4 spiny neurons (L4SPs). The physiology data (i.e., AP responses to passive deflections of the principal and its eight adjacent whiskers (de Kock et al., 2007)) were grouped by the hence determined morphological cell types, resulting in cell type-specific wRFs.

Multi-compartmental model

We generated a biophysically-detailed multi-compartmental neuron model, which captures the stereotypic morphological and intrinsic physiological properties of L5PTs. The L5PT model is based on the 3D soma-dendrite reconstruction of a L5PT neuron, whose morphological and topological features – which allow discriminating L5PTs from other excitatory cell types in the deep layers (see above) – represent approximately the respective averages across a population of 37 L5PTs (Narayanan et al., 2015; Rojas-Piloni et al., 2017) that were labeled *in vivo* via cell-attached recordings in layer 5 of rat vS1. A simplified axon morphology was attached to the reconstructed soma based on Hay et al. (2013). The axon consisted of an axon hillock with a diameter tapering from 3 μm to 1.75 μm over a length of 20 μm, an axon initial segment (AIS) of 30 μm length and diameter tapering from 1.75 μm to 1 μm diameter, and 1 mm of myelinated axon (diameter of 1 μm). The diameter of the reconstruction of the apical trunk and oblique dendrites was scaled by a factor of 2.5 to allow for backpropagation of action potentials (bAP), and bAP-triggered calcium spike (BAC) firing to occur (i.e., after scaling the diameter of the apical trunk was 4.5 μm at the soma, and 1.5 μm at the main bifurcation located at a distance of $\sim$900 μm from the soma). Spatial discretization of the dendrite morphology (i.e., compartmentalization) was performed by computing the electrotonic length constant of each dendrite branch at a frequency of 100 Hz and setting the length of individual compartments in this branch to 10% of this length constant. The length of axonal compartments was set to 10 μm. After spatial discretization, the L5PT morphology consisted of 1,033 compartments with an average length of $\sim$15 μm, but no longer than 42 μm. The resultant L5PT model was then combined with previously reported biophysical models of a variety of Hodgkin-Huxley (HH)-type ion channels (Table S2) that are expressed at different densities within the soma, basal and/or apical dendrites, and axon initial segment (Hay et al., 2011). Using an evolutionary multi-objective optimization algorithm (Druckmann et al., 2007), we tuned the parameters of the biophysical models until numerical simulations of the L5PT model (using NEURON 7.2 (Hines and Carnevale, 1997)) reproduced current injection-evoked somatic and/or dendritic sub- and suprathreshold responses that are characteristic for L5PTs, as measured previously via whole-cell recordings in acute brain slices of rat vS1 *in vitro* (Hay et al., 2011). Fixed membrane parameters were the axial resistance (100 Ωcm in all compartments), the membrane capacitance (1 μF/cm^2 at the soma and axon, 2 μF/cm^2 in the apical and basal dendrites to account for increased surface area due to spines, and 0.04 μF/cm^2 along the myelinated part of the model axon), and the passive membrane conductance along the myelinated part of the axon (g_{pas} = 0.4 pS/μm^2, i.e., equivalent to a specific membrane resistance of 25,000 Ωcm^2). The reversal potential of the passive membrane conductance was set to $-$90 mV. Conductance densities of the non-specific cation current I_h were fixed at 0.8 pS/μm^2 in the soma and axon, and 2 pS/μm^2 in the basal dendrites. In the apical dendrite, the conductance density of I_h increased exponentially with the distance to the soma. The biophysical model parameters to be optimized were the peak conductance per unit membrane area for various voltage-dependent ion channels, and the parameters of a phenomenological model of the calcium dynamics in different parts of the morphology (i.e., axon, soma, basal and apical dendrites; Table S2). The targets of the optimization were different features of the membrane potential in response to two stimuli, as measured previously (Hay et al., 2011): (1) a brief current injection into the soma should trigger an AP at the soma and a bAP, and (2) a brief current injection into the soma, followed by current injection into a Ca^{2+} channel dense region around the first bifurcation point of the apical tuft, should trigger somatic bursts (i.e., BAC firing). The specific features, as listed in Table S3, were combined into five objectives, which were then optimized simultaneously by using the evolutionary algorithm (Druckmann et al., 2007). A set of 1,000 models was generated with parameters drawn randomly from a physiologically plausible range. In every iteration, each model was then evaluated by simulating the response to the two stimuli, calculating the features and determining the error by calculating the difference between each simulated and measured feature in units of standard deviations of the experimental feature (Hay et al., 2011). After each model had been evaluated, a new set of 1,000 models was generated from the previous set by stochastically transferring parameter values from "good" models (i.e., lower errors) to "worse" models (i.e., higher errors). Additionally, parameter values of all models were updated stochastically to avoid converging to local minima. This procedure was repeated 500 times. From the final iteration, the set of biophysical models used here was selected based on three criteria: (1) it

had the lowest sum across all objective errors, (2) similar deviations in all objective errors (i.e., models where only a subset of objectives matched the experimental data were not considered), and (3) it supported regular spiking of increasing frequencies in response to sustained current injections of increasing amplitude.

Connectivity model

The structurally plausible constraints for the numbers and dendritic distributions of cell type-specific synaptic input patterns that impinge onto the L5PT model are based on an anatomically realistic network model of rat vS1, as described in detail previously (Egger et al., 2014). Briefly, we generated a 3D model of the average geometry of rat vS1 (i.e., 3D location, orientation and diameter of all barrel columns; 3D pial and white matter (WM) surfaces), and determined the variability (~50 μm) of these anatomical landmarks across twelve animals (Egger et al., 2012). Next, we measured the number and 3D distribution of all excitatory and inhibitory neuron somata in rat vS1 (~530,000 neurons) and the ventral posterior medial nucleus (VPM) of the thalamus (~6,000 neurons) in four different animals (Meyer et al., 2013), and generated an average excitatory and inhibitory 3D neuron somata distribution at a resolution of 50x50x50 μm^3, reflecting the variability of the cortex geometry across animals. We then registered a sample of 177 excitatory intracortical (IC) neuron morphologies (i.e., grouped into ten cell types (see above) (de Kock et al., 2007; Narayanan et al., 2015), 14 excitatory thalamocortical (TC) axon morphologies labeled in VPM *in vivo* (Oberlaender et al., 2012b), and 213 inhibitory neuron (IN) morphologies (203 labeled in layers 2 to 6 *in vitro* (Arzt et al., 2018; Helmstaedter et al., 2009; Koelbl et al., 2015), 10 labeled in L1 *in vivo* (Egger et al., 2015)) to the geometric model of vS1. Combining these data by using a previously reported network building approach (Egger et al., 2014), we generated a structurally dense model of vS1, which comprised soma, dendrite and axon morphologies that represent all of the excitatory (here: 462,402) and inhibitory neurons (here: 67,535) that are located in rat vS1, as well as axon morphologies that represent the IC part of all VPM neurons (here: 6,225). To estimate synaptic connectivity within this structurally dense vS1 model, we calculated the overlap at 50 μm^3 resolution between the putative postsynaptic target structures (PSTs; i.e., soma/dendrite surface for inhibitory connections; dendritic spines for excitatory connections) and putative presynaptic sites (i.e., axonal boutons) for all pairs of neurons, and normalized this quantity by the respective total amount of locally available PSTs (i.e., total somatic/dendritic surface and number of spines within each 50 μm voxel). Neglecting wiring specificity at subcellular scales (Egger et al., 2014), we converted these overlap measurements into connection probabilities, which predict the respective distributions of the numbers and most likely dendritic locations of synaptic contacts. To compare the predicted connection probabilities between excitatory IC cell types and L5PTs with previously reported paired-recording results that were obtained from acute brain slices *in vitro* (Lefort et al., 2009; Thomson et al., 2002; Brown and Hestrin, 2009; Perin et al., 2011; Song et al., 2005; Thomson et al., 1996), we cropped out ten 300 μm wide thalamocortical/semi-coronal slices from the network model, which comprised at least half of the C2 barrel column volume. Connection probabilities that were predicted for truncated morphologies in slices are denoted by asterisks in Table S1. Finally, we embedded the L5PT model into the network model of vS1 by using a previously reported registration approach (Egger et al., 2012). Here, we placed the L5PT model at nine different locations within the barrel column representing the C2 whisker (i.e., approximately in the center of vS1), while preserving its (*in vivo*) soma depth location. For each of the nine locations (i.e., one in the column center, and eight at equally spaced angular intervals with a distance of ~100 μm to the column center) we used the connectivity mapping procedures as described above to estimate the numbers and dendritic locations of cell type-specific synaptic inputs that impinge onto the dendrites of the L5PT model. Specifically, by sampling from the overlap distributions 50 times, calculating the mean of the number of synaptic inputs from each cell type, and choosing the sample that was closest to this mean, we estimated that the L5PT model receives a total of 24,161 ± 785 synaptic inputs. Of those, ~90% are predicted to originate from excitatory IC and TC neurons, which corresponds to an average density of 1.4 glutamatergic and 0.14 GABAergic synapses per μm dendrite, respectively (i.e., 148 ± 18 GABAergic synapses are located on the soma).

Synapse models

Conductance-based synapses were modeled with a double-exponential time course. Excitatory synapses contained both AMPA receptors (AMPARs) and NMDARs. Inhibitory synapses contained $GABA_A$Rs. The reversal potential of AMPARs and NMDARs was set to 0 mV, that of $GABA_A$Rs to −75 mV. Rise and decay time constants of AMPARs were set to 0.1 ms and 2 ms, respectively (Feldmeyer et al., 2002); those of NMDARs to 2 ms and 26 ms, respectively (Feldmeyer et al., 2002); and those of $GABA_A$Rs to 1 ms and 20 ms, respectively (Wozny and Williams, 2011). The Mg-block of NMDARs was modeled by multiplying the conductance value with an additional voltage-dependent factor $1/(1 + \eta \cdot \exp(-\gamma \cdot V))$ (Jahr and Stevens, 1990), where $\eta = 0.25$, $\gamma = 0.08/mV$, and V is the membrane potential in mV (Larkum et al., 2009). The peak conductance at excitatory synapses from different presynaptic cell types was determined by assigning the same peak conductance to all synapses of the same cell type, activating all connections of the same cell type (i.e., all synapses originating from the same presynaptic neurons) one at a time, and comparing parameters of the resulting unitary postsynaptic potential (uPSP) amplitude distribution (mean, median and maximum) for a fixed peak conductance with experimental measurements *in vitro* (input from layers 2 to 6 (Schnepel et al., 2015)) or *in vivo* (TC input (Constantinople and Bruno, 2013)). The peak conductance for synaptic inputs from each cell type was systematically varied until the squared differences between parameters of the *in silico* and *in vitro*/*in vivo* uPSP amplitude distributions were minimized (i.e., the mean, median and maximum of the distributions were used, and mean and median were weighted twice relative to the maximum) (Table S4). The peak conductance at inhibitory synapses was fixed at 1 nS (Hay and Segev, 2015). Release probability at excitatory and inhibitory synapses was fixed at 0.6 and 0.25, respectively (Gupta et al., 2000; Hay and Segev, 2015).

Synaptic input patterns

Synaptic input patterns to the L5PT model were estimated as follows: All presynaptic neurons determined during the network-embedding procedure were converted into point neurons that could emit APs. During periods of ongoing activity, APs in presynaptic neurons were modeled as Poisson trains with cell type-specific mean firing rates as measured *in vivo* (Oberlaender et al., 2012a). The mean firing rate of INs was set to 7 Hz (Hay and Segev, 2015) (except for L1 INs (Egger et al., 2015)). Each AP in a presynaptic neuron is registered at all synapses between the presynaptic neuron and the L5PT model without delay and may cause a conductance change, depending on the release probability of the synapse. After a stimulus (i.e., deflection of the PW, SW or 2nd SW), each presynaptic neuron can emit additional spikes. The location of the deflected whisker in the wRF of the presynaptic neuron is determined based on the barrel column where the soma of the presynaptic neuron is located in (i.e., a convolution operation), and the corresponding whisker-specific post-stimulus time histogram (PSTH) is used to stochastically generate additional sensory-evoked APs. Whisker-specific PSTHs of excitatory cell types were generated based on *in vivo* wRF measurements (Figure S3). The amplitude of the PSTH of excitatory IC cell types is further scaled by a factor of 0.4571 to reflect lower response probabilities of cortical neurons in the up-state (Petersen et al., 2003). The whisker-specific PSTHs of TC neurons in VPM were constructed based on previously published *in vivo* measurements, where single- and multi-whisker responsive neurons were described for the same experimental conditions used in this study (Brecht and Sakmann, 2002). Single- and multi-whisker responsive VPM neurons were grouped into a single TC PSTH. The whisker-specific PSTHs of INs in vS1 were constructed based on previously published *in vivo* measurements, which were acquired under the same experimental conditions that were used here (Bruno and Simons, 2002; Reyes-Puerta et al., 2015), and which can be summarized as follows: (1) the onset times of whisker-evoked APs in INs across all layers should be similar to those of the excitatory cell types; (2) in case of PW touch, AP onset times in INs should precede those of the excitatory IC, but not TC cell types; (3) INs have broad wRFs. To capture these empirical constraints, the PW/SW evoked PSTHs of INs were set to the respective maximum values across all excitatory cell types in each 1 ms time bin; the resultant PW evoked PSTH was shifted by −1 ms (but no spiking before TC neurons; i.e., > 8 ms); and the ratio between the integrals of the PW- and SW evoked PSTHs during 0-50 ms was set to a fixed ratio of 2:1. These constraints leave one free parameter for constructing the PSTHs of INs: the total number of PW evoked APs during 0-50 ms post stimulus. We simulated the response of the L5PT model after PW deflections while systematically varying this parameter, and computed the resulting number of APs during 0-25 ms, until the L5PT model exhibited simulation trials with and without AP responses as measured *in vivo*. This yielded a value for INs of 1.0 APs per PW deflection per 50 ms.

Simulations

We generated 200 samples of structurally- and functionally-plausible cellular stimulus representations for each of the nine L5PT model locations (i.e., 1,800 samples per whisker), for each simulated whisker deflection in the control condition (i.e., the complete network model) and in conditions where sensory-evoked synaptic input from different presynaptic IC and TC populations was removed (i.e., sensitivity analysis), and for two different *in silico* pharmacology experiments. Since the L5PT models were located in the C2 column, simulated C2 deflections were assigned as PW deflections, those of the eight adjacent whiskers as SW deflections, and simulated E2 deflections as 2nd SW deflections. The four different conditions of the sensitivity analysis were as follows (Figure 4D): (1) stimulus-evoked APs of all L3PYs and L4SPs were removed; (2) stimulus-evoked APs of all L5PTs were removed; (3) stimulus-evoked APs of all L6CCs were removed; (4) stimulus-evoked APs of all L6CCs and TC neurons were removed. The two different *in silico* pharmacology conditions were as follows (Figure 5A): (1) synapses from L6CCs whose somata were located within the E2 column or the surrounding septum were removed from the L5PT model; (2) synapses from neurons of all excitatory cell types whose somata were located within the E2 column, except for L6CCs, were removed. All combinations of L5PT model location, identity of the deflected whisker, sensitivity and pharmacology condition resulted in 126,000 spatiotemporal synaptic input patterns, which we associate with different trials. For each trial, we numerically simulated the integration of the respective conductance changes within all dendritic compartments (and the soma and axon) of the HH-type L5PT model. Each simulation trial consisted of 245 ms ongoing activity, followed by 50 ms of sensory-evoked activity. The first 100 ms and the last 25 ms of simulated activity were discarded. AP times were determined from zero-crossings of the simulated membrane potential at the soma. For each of the simulation trials (control condition) we created a 100-dimensional vector, which quantified the spatiotemporal features of the respective synaptic input patterns that impinge onto the L5PT model. Entries of the vector represented all active synapses during the period of 0-25 ms post stimulus, their respective path length distances to the soma, times of activation with 1 ms resolution, and whether the synapses originated from excitatory or inhibitory neurons. The input vectors were sorted into two groups, representing simulations in which onset APs (i.e., during the period of 8-25 ms post stimulus) did or did not occur. A principal component analysis (PCA) of these spatiotemporal input vectors revealed that trials with versus without onset APs formed overlapping, but systematically different distributions. PC_1 discriminated between these distributions. 92% of PC_1 could be accounted for by the excitatory and inhibitory inputs that are active during a period of 8-16 ms post stimulus, and that are located within less than 500 μm path length distance to the soma (here referred to as proximal inputs). We therefore defined a single quantity – synchronous proximal drive (SPD) – reflecting the net input (i.e., number of active excitatory minus the number of active inhibitory synapses) along the proximal dendritic compartments of the L5PT model (i.e., path length distance < 500 μm) within 8-16 ms. We then calculated the probability of observing a whisker-evoked AP response in the L5PT model as a function of SPD, and fitted a sigmoidal curve to this distribution. The inverse width (or slope) of the fitted sigmoidal curve can be interpreted as a measure for the predictive power of SPD for AP responses. We systematically varied the end time point of the integration time window to determine the SPD window with highest predictive power,

which matched closely with the SPD window determined for PW deflections by the PCA. These SPD windows were then used to compute the AUROC values for PW and SW deflections. Breaking down SPD into its two parameters, (1) the number of active excitatory synapses along the proximal dendrites, and (2) their respective synchrony (i.e., time window in which they are active), we performed additional simulations of the L5PT model. The parameters of the biophysical properties of the multi-compartmental model, the synapse models and the synaptic input patterns preceding the stimulus remained unchanged. The structurally and functionally constrained PW/SW-evoked spatiotemporal synaptic input patterns were replaced as follows. First, the distribution of stimulus-evoked synaptic inputs along the dendrites of L5PT model was determined by calculating the average distribution of active synapses during 50 ms following PW and SW simulation trials (i.e., from the structurally and functional constrained trials). Second, the resultant 3D distributions of active excitatory and inhibitory synapses were converted into distance-dependent probability distributions (i.e., 1D) with 50 μm (i.e., path length) resolution. Third, the subcellular distributions, temporal activation patterns and numbers of active synapses (i.e., excitatory/inhibitory during periods of ongoing activity; inhibitory during periods of whisker-evoked activity) were then determined by calculating the respective averages across PW and SW simulation trials (i.e., from the structurally and functional constrained trials), respectively. Fourth, the temporal distribution of active excitatory synapses was modeled as a log-normal distribution (de Kock et al., 2007) with a fixed offset of 8 ms post-stimulus (i.e., corresponding to the onset latency of VPM input) and a fixed peak time of 9 ms post-stimulus. Fifth, the only remaining parameter was the median timing of the log-normal distribution. Varying this parameter in 1 ms steps resulted in excitatory synaptic input distributions that ranged from highly synchronous (2 ms; i.e., median timing at 10 ms post stimulus) toward asynchronous (i.e., median timing much later than 10 ms post stimulus). Sixth, at the same time, the total number of active excitatory synaptic inputs was systematically varied. Seventh, for each combination of the number and synchrony of stimulus-evoked excitatory inputs, 200 samples of spatiotemporal synaptic input patterns were generated and simulated as described above. Then, the probability of an onset AP (i.e., between 8-16 ms) was calculated for each combination of the number and synchrony of stimulus-evoked excitatory inputs. Iso-AP probability contour plots were calculated by arranging all synaptic input number and synchrony combinations in a 2D grid, and linear interpolation between the grid points. The corresponding *in vivo* data of cell type-specific numbers and synchronies of active proximal inputs were derived from the structural and functional simulation constraints of PW, SW and 2nd SW deflections. For calculating the gain that TC and each of the different IC cell types contribute to AP responses of the L5PT models, all stimulus-evoked APs from neurons of the respective presynaptic cell type were removed. For each excitatory cell type and cell type combinations, 1,800 simulation trials were performed for PW, SW and 2nd SW, respectively. Cell type-specific gain was defined as the ratio between the average numbers of APs within 0–25 ms post stimulus during control and manipulated simulations. The contribution to the fast onset APs that is provided by L6CCs was defined as the fraction of stimulus-evoked L6CC synapses within the time window defined by the SPD analysis relative to all active L6CC and TC synapses (i.e., that are required to drive APs). To quantify the contributions by L6CCs from individual barrel columns, only synaptic inputs from L6CCs that were located within/around the barrel column that was somatotopically aligned with the stimulated whisker were considered.

QUANTIFICATION AND STATISTICAL ANALYSIS

All data are reported as mean ± standard deviation (SD) unless mentioned otherwise. All of the statistical details can be found in the figure legends, figures, and Results, including the statistical tests used, exact value of n, what n represents (e.g., number of animals, number of cells), and precision measures (e.g., confidence intervals). Normality was not assumed when performing statistical testing. Significance was defined for p values smaller than 0.05. All tests were performed using the R software package (version 3.4.3) and the scipy python package (version 1.0.1).

DATA AND CODE AVAILABILITY

All relevant data are available from the authors. The model and simulation routines, including a detailed documentation of all parameters and the analysis routines can be obtained from ModelDB (https://senselab.med.yale.edu/ModelDB/; accession number: 239145).

Neuron, Volume *105*

Supplemental Information

Cortical Output Is Gated by Horizontally Projecting Neurons in the Deep Layers

Robert Egger, Rajeevan T. Narayanan, Jason M. Guest, Arco Bast, Daniel Udvary, Luis F. Messore, Suman Das, Christiaan P.J. de Kock, and Marcel Oberlaender

Supplemental Videos

Video S1 (related to Figure 3): Examples of *in silico* wRF mappings in L5PT model.

Supplemental Figures

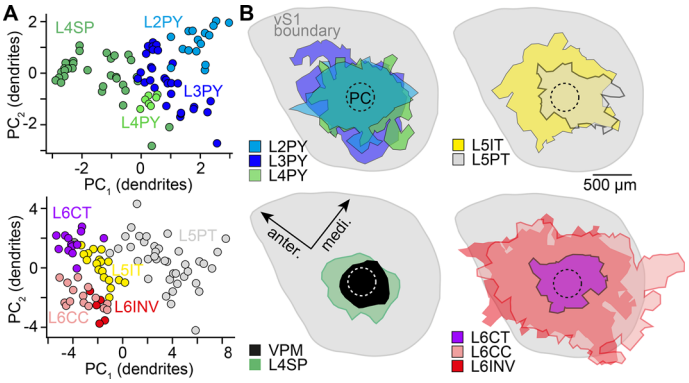

Figure S1 (related to Figure 1): Classification of *in vivo* labeled neurons into axo-dendritic cell types. A) Principal components ($PC_{1/2}$) of dendritic features (see (Narayanan et al., 2015)) that discriminate between axo-dendritic cell types in the upper and deep layers, respectively. **B)** Horizontal axon extent for each axo-dendritic cell type (i.e., the respective somata are located within the principal barrel column representing the C2 whisker (PC)).

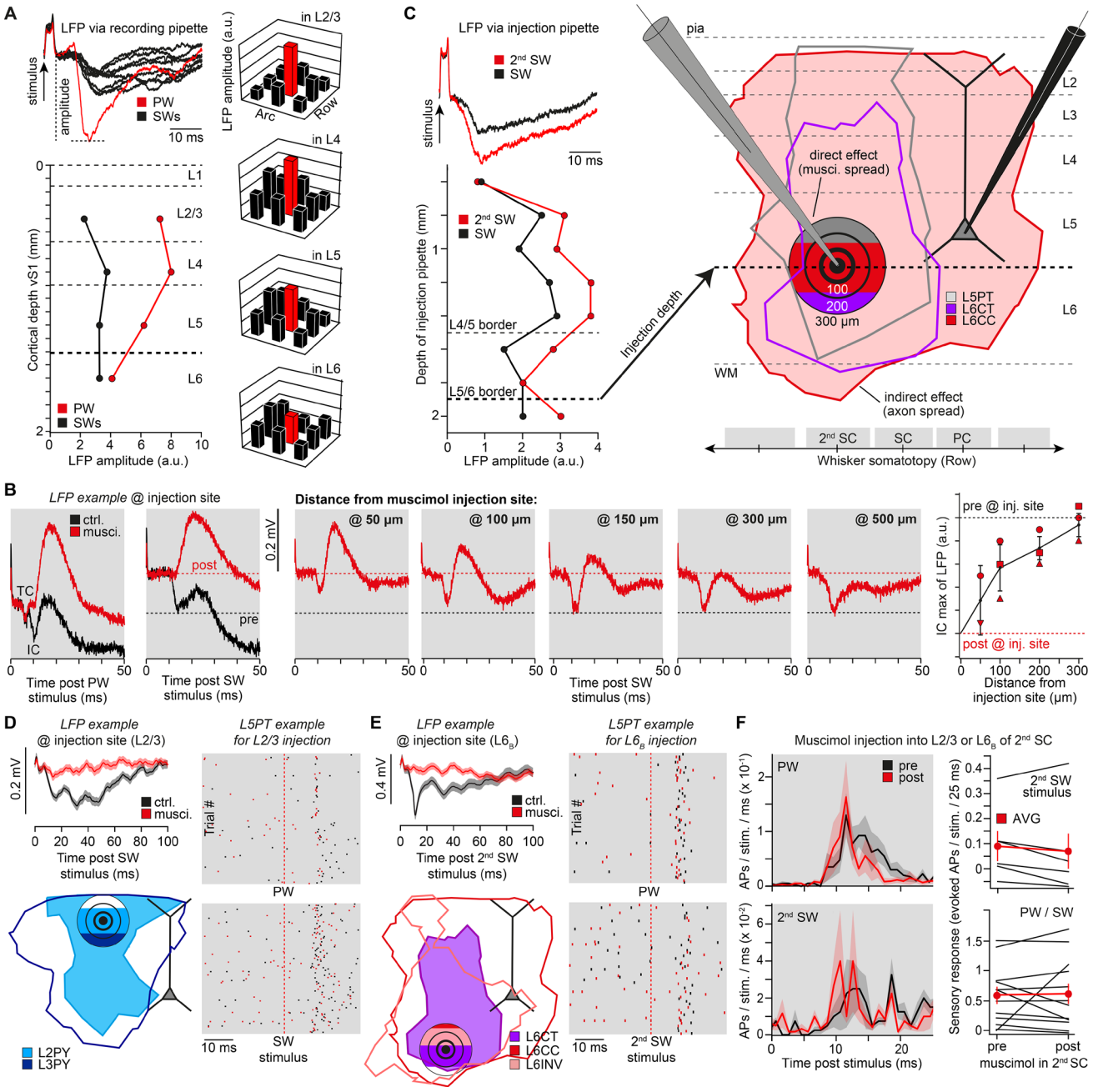

Figure S2 (related to Figure 5): LFP guided *in vivo* pharmacology. A) Left panel: LFP recordings via search pipette at 400 µm depth in vS1. LFP amplitudes in response to deflections of the PW and its eight SWs were quantified. Right panel: LFP wRF reveals the PW at the recording site (Lee et al., 2015) (here: C2). LFP wRF measurements were repeated at different cortical depths of vS1. Using the depth of layer borders (Meyer et al., 2013), the characteristic laminar profiles of LFP responses to PW (and SW) stimuli were used to identify the border between layer 4 and 5 (i.e., ~100 µm below the LFP maximum). The target location at the layer 5/6 border was hence approximately 400-500 µm below the LFP maximum. **B)** Complete deactivation of IC activity by muscimol injections was restricted to a volume of less than 100 µm in diameter. Injections had no direct pharmacological effect on neurons more distant than 300 µm from the injection site (i.e., no muscimol spread to layer 4 or the adjacent SCs). **C)** Example experiment

that illustrates how the LFP depth profile was used to locate the L5/6 border of the barrel column representing the manipulated 2nd SW (here: E2). The muscimol injection pipette was inserted rostral to vS1 at an angle that was approximately parallel to the midline (i.e., oblique to the vertical axis of vS1). E2 was identified as the manipulated 2nd SW based on the larger LFP amplitudes across the cortical depth when compared to those evoked by SW stimuli (shown here: E1). The target location (i.e., layer 5/6 border) was then determined by identifying the depth of maximal LFP amplitude and adding 500 µm (i.e., here injection at ~1,850 µm depth). Before and after muscimol injections, APs of L5PTs were recorded, whose respective PWs were separated by one whisker from the manipulated one (e.g. PW at the recording site is B2, the manipulated 2nd SW is D2, and the separating whisker is C2). Axonal extent from neurons located in the 2nd SC show that only L6CCs within the injection volume could directly impact L5PT responses at the recording site. **D)** Example LFPs before and after muscimol injections, recorded at the injection site around the border between layer 2 and 3. Corresponding AP responses in layer 5 evoked by the PW and manipulated whisker. Axonal extent from neurons located in the 2nd SC show that primarily L3PYs within the injection volume could directly impact L5PT responses at the recording site. **E)** Example LFPs before and after muscimol injections, recorded at the injection site in deep layer 6 (~1,800 µm underneath the pial surface). Corresponding AP responses in layer 5 evoked by the PW and manipulated whisker. Axonal extent from neurons located in the 2nd SC show that L6INVs within the injection volume could directly impact L5PT responses at the recording site. **F)** PW and 2nd SW evoked PSTHs across recorded L5PTs (n=6) before and after muscimol injections into layers 2/3 or deep layer 6 of the respective 2nd SC. Right panels: response per L5PT to stimulation of the 2nd SW and non-manipulated whiskers (i.e., PW and SW) before and after muscimol injections (mean ± SEM). Panels D-F are analogous to those shown for injections at the layer 5/6 border in **Figure 5**.

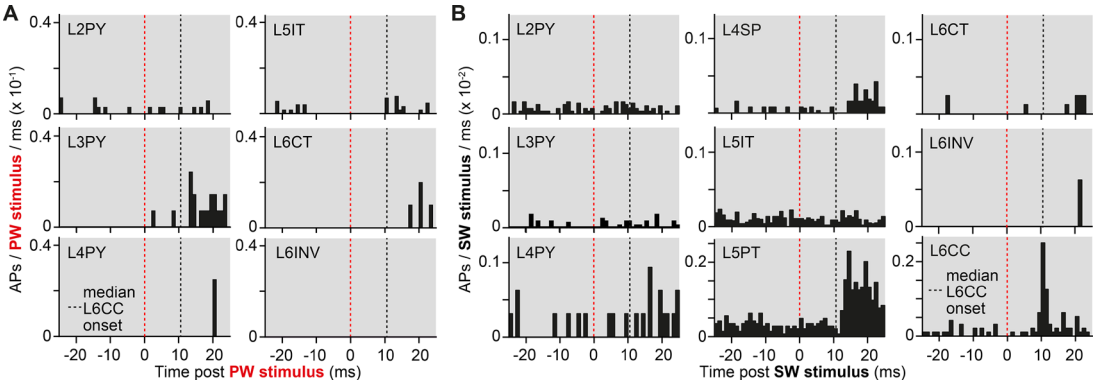

Figure S3 (related to Figure 7): Cell type-specific functional constrains for *in silico* experiments. **A)** PSTHs of PW evoked APs for morphologically classified neurons: L2PY (n=7), L3PY (n=7), L4PY (n=2), L5IT (n=13), L6CT (n=5) and L6INV (n=1), analogous to those shown in **Figure 7C** for L4SPs, L5PTs and L6CCs. **B)** PSTHs of SW evoked APs for all cell types (i.e., averaged across the eight SWs), representing the cells shown in panel A, **Figures 1** and **7C**.

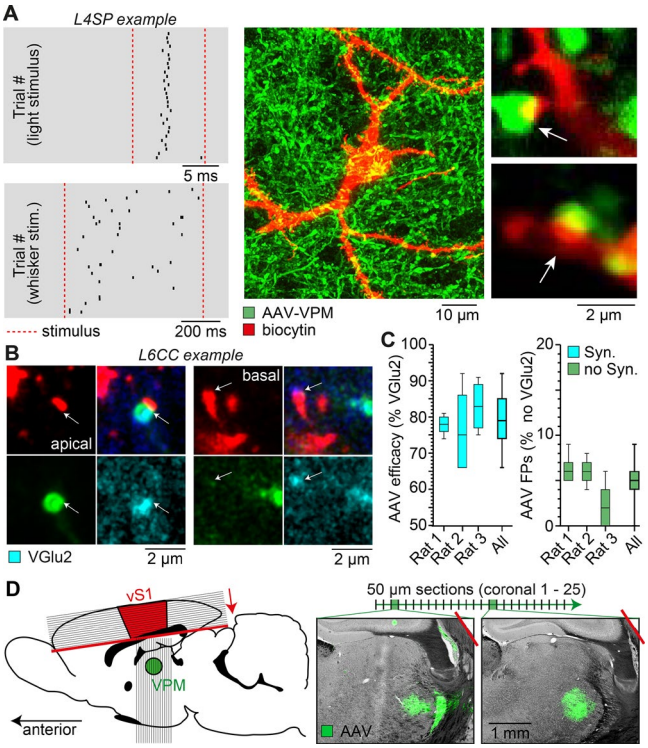

Figure S4 (related to Figure 8): Quantification of AAV injections. A) Example of cell-attached *in vivo* recording in layer 4 of AAV-injected brain. Ticks represent APs in response to a 10 ms flash of green light onto the cortical surface and a 700 ms airpuff onto the whiskers, respectively. Confocal images identify the recorded neuron as a L4SP. Putative TC synapses were identified as contacts between VPM boutons and dendritic spines. **B)** Super-resolution microscopy of the L6CC shown in **Figure 8**. Left panels show exemplary TC synapse along the apical dendrite (i.e., co-localized with VGlu2). Right panel shows exemplary TC synapse that was not labelled by the AVV injection into the VPM. **C)** Left panel: Fractions

of VGlu2-positive boutons (n=884) in layer 4 and at the layer 5/6 border of vS1 that were infected by AAV injections into the VPM (i.e., efficacy of the AAV is ~80%). Right panel: Fractions of the AAV-positive swellings (n=739) that were identified as TC boutons, but which did not co-express VGlu2 (i.e., false positive (FP) TC synapses). **D)** AAV injections sites for the L6CC shown in **Figure 8**. Cortex was cut into consecutive sections tangentially to vS1, the rest of the brain was cut coronally.

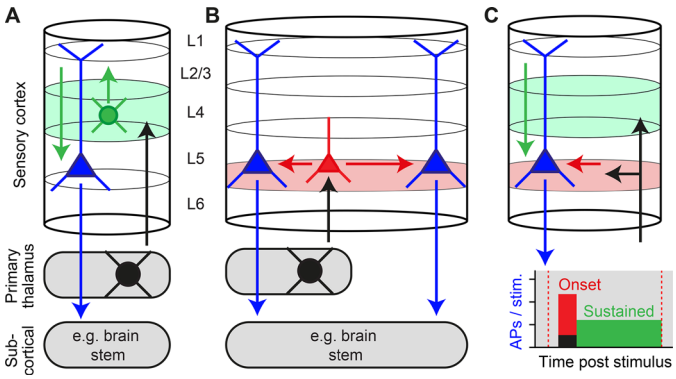

Figure S5 (related to Figure 8): Suggested concept of primary sensory cortex. Sensory-evoked TC input is relayed in parallel by two orthogonally organized thalamorecipient populations which give rise to complementary canonical pathways: vertical to layers 2/3 by L4SPs **(A)**, and horizontally to layers 5/6 by L6CCs **(B)**. The deep thalamorecipient pathway activates L5PTs, whereas signal flow in the upper layers terminates in layer 5. **C)** The complementary pathway theory hence provides a potential explanation for sustained AP responses in L5PTs that persist for the duration of the stimulus. We showed that one way to drive cortical output is by providing sufficiently strong and synchronous synaptic input to the proximal dendrites. However, synchrony decreases during recurrent excitation within local and long-range cortical circuits. Moreover, a substantial fraction of these recurrent and top-down inputs will impinge onto distal dendrites (e.g. within layer 1). It is hence unlikely that sustained responses in L5PTs originate from the same mechanism as the onset responses (see also (Rojas-Piloni et al., 2017)). We thus hypothesize that the L6CC gated onset responses are required to switch the apical dendrites into an active state, which allows L5PTs to transform temporally less synchronous and spatially more distributed synaptic inputs (e.g. from layers 2/3) into sustained patterns.

Supplemental Tables

Presynaptic cell type	Measurement (Reference)	Network model (L5PT population)	Network model (L5PT model)
L2PY	0.08 (Lefort et al., 2009)	0.07 ± 0.09*	0.13 ± 0.02
L3PY	0.12/0.55 (Lefort et al., 2009, Thomson et al., 2002)	0.15 ± 0.16*	0.34 ± 0.02
L4 (SP, PY)	0.08 (Lefort et al., 2009)	0.14 ± 0.15*	0.33 ± 0.04
L5IT	0.19 (Brown and Hestrin, 2009)	0.17 ± 0.13*	0.19 ± 0.05
L5PT	0.05-0.2 (Brown and Hestrin, 2009, Perin et al., 2011, Song et al., 2005)	0.23 ± 0.19*	0.24 ± 0.06
L6 (CC, INV, CT)	0.02 (Lefort et al., 2009)	0.13 ± 0.14*	0.15 ± 0.02
VPM	0.44 ± 0.17 (Constantinople and Bruno, 2013)	0.40 ± 0.12	0.39 ± 0.05
INH	0.22 (Thomson et al., 1996)	0.41 ± 0.14	0.26 ± 0.02

Table S1 (related to Figure 2). Cell type-specific connection probabilities. Comparison between predicted connection probabilities in vS1 network model and previously reported measurements from paired-recordings *in vitro* or *in vivo* (mean ± STD). The * denotes predicted connection probabilities between truncated morphologies in 300 µm thick thalamocortical/semi-coronal slices of the network model, because the respective empirical data was acquired in 300 µm thick acute brain slices *in vitro*.

Parameter	Soma	AIS / Myelin	Apical dendrite	Basal dendrites
C_m (μF/cm^2)	1.0	1.0 / 0.04	2.0	2.0
r_a (Ωcm)	100	100 / 100	100	100
g_{pas} ($1/r_m$)	0.326	0.256 / 0.4	0.882	0.631
Na_t	24300	880 / –	252	–
Na_p	49.9	14.6 / –	–	–
K_t	471	841 / –	–	–
K_p	0	7730 / –	–	–
SKv3.1	9830	9580 / –	112	–
SK E2	492	0.577 / –	34	–
Ca_{LVA}	46.2	85.8 / –	1040*	–
Ca_{HVA}	6.42	6.92 / –	45.2*	–
τ_{Ca} (ms)	770	507 / –	133	–
γ_{Ca} (1)	0.000616	0.0175 / –	0.0005	–
I_m	–	– / –	1.79	–
I_h	0.8	0.8 / –	$A+B\cdot\exp(C\cdot d/d_{max})$ **	2

Table S2 (related to Figure 3). Biophysical parameters of the L5PT model. These parameters were obtained using the multi-objective optimization algorithm described previously (Druckmann et al., 2007, Hay et al., 2011). Units for different ion channel densities are pS/μm^2. τ_{Ca} (ms) is the time constant of the calcium buffering model, and γ_{Ca} is a dimensionless parameter describing the calcium buffer affinity. g_{pas}: passive membrane conductance; Na_t: fast inactivating sodium current; Na_p: persistent sodium current; K_t: fast inactivating potassium current; K_p: slow inactivating potassium current; SKv3.1: fast non-inactivating potassium current; SK E2: calcium-activated potassium current; Ca_{LVA}: low voltage-activated calcium current; Ca_{HVA}: high voltage-activated calcium current; I_m: muscarinic potassium current; I_h: non-specific cation current. * Density in the calcium "hot zone" between 900-1100 μm from the soma. The density of low- and high-voltage activated calcium channels in the apical dendrite was set to 1% and 10% of that value, respectively, outside of the "hot zone". ** The density of I_h in the apical dendrite increases exponentially with distance d to the soma, with parameters A = -0.8696 pS/μm^2, B = 2.087pS/μm^2, C=3.6161, and d_{max} the distance of the apical dendrite top located the furthest from the soma. Voltage- and time-dependence of ion channels was modeled using the HH formalism. All corresponding parameters were taken from the literature and have been described in detail previously (Hay et al., 2011).

Feature	Mean ± STD	Model	Difference (STD)
Ca^{2+} AP peak	6.73 ± 2.54 mV	10.8 mV	1.6
Ca^{2+} AP width	37.43 ± 1.27 ms	36.5 ms	0.7
BAC AP count	3 ± 0	3	0
Mean somatic AP ISI	9.9 ± 0.85 ms	9.4 ms	0.6
Somatic AHP depth	−65 ± 4 mV	-66 mV	0.3
Somatic AP peak	25 ± 5 mV	34 mV	1.8
Somatic AP half-width	2 ± 0.5 ms	1.6 ms	0.8
AP count (somatic current injection only)	1 ± 0	1	0
bAP amplitude at 835 µm from the soma	45 ± 10 mV	14 mV	3.1
bAP amplitude at 1015 µm from the soma	36 ± 9.33 mV	9 mV	2.9

Table S3 (related to Figure 3). Optimization targets for biophysical L5PT models. Features of membrane potential used to constrain the intrinsic physiology of the L5PT models. Empirical features were adapted from (Hay et al., 2011). ISI: inter-spike interval; AHP: after-hyperpolarization. Model features based on optimized parameters. Difference between model features and average experimental features given in units of STD of the experimental features.

Cell type	uPSP Mean (mV) (exp. / fit)	uPSP Median (mV) (exp. / fit)	uPSP Max. (mV) (exp. / fit)	Conductance per synapse (nS)
L2PY	0.49 / 0.43	0.35 / 0.37	1.90 / 2.50	1.47
L3PY	0.49 / 0.44	0.35 / 0.39	1.90 / 1.98	1.68
L4 (SP, PY)	0.35 / 0.35	0.33 / 0.30	1.00 / 1.41	1.14
L5IT	0.47 / 0.40	0.33 / 0.35	1.25 / 1.70	1.38
L5PT	0.46 / 0.43	0.36 / 0.39	1.50 / 1.46	1.59
L6(CC, INV)	0.44 / 0.42	0.31 / 0.40	1.80 / 1.26	1.63
L6CT	0.44 / 0.39	0.31 / 0.36	1.80 / 1.73	1.80
VPM	0.571 / 0.51	0.463 / 0.44	1.18 / 1.80	1.78

Table S4 (related to Figure 3). Cell type-specific synaptic strengths. Features of uPSP distributions of L5PTs for synaptic input from each presynaptic excitatory cell type, and the respectively fitted synaptic conductance values. Empirical values for uPSP amplitude distributions of synapses from IC cell types (Schnepel et al., 2015) and VPM thalamus (Constantinople and Bruno, 2013) were adapted as reported previously.